An Overview of Emerging 2D Nanomaterials: General Synthesis Methods and Properties

Ravi Anusuyadevi, P.; Pranavi, Sindhu; Shaw, Roushan Nigam Ramnath ; Mádai, E.; Prasanna Kumar, Darsi Jaya; Gonugunta, P.; Taheri, P.; Mol, J.M.C.

DOI
10.1039/9781837675838-00001

Publication date
2025

Document Version
Final published version

Published in
Next-generation 2D Nanomaterials for Sustainable Energy and Environment-oriented Applications

Citation (APA)
Ravi Anusuyadevi, P., Pranavi, S., Shaw, R. N. R., Mádai, E., Prasanna Kumar, D. J., Gonugunta, P., Taheri, P., & Mol, J. M. C. (2025). An Overview of Emerging 2D Nanomaterials: General Synthesis Methods and Properties. In N. Singh, & A. Kumar (Eds.), *Next-generation 2D Nanomaterials for Sustainable Energy and Environment-oriented Applications: Electrocatalysis, Photoelectrocatalysis and Photocatalysis* (pp. 1-67). (Nanoscience & Nanotechnology Series; Vol. 66). RSC Publishing. https://doi.org/10.1039/9781837675838-00001

CHAPTER 1

An Overview of Emerging 2D Nanomaterials: General Synthesis Methods and Properties

PRASAANTH RAVI ANUSUYADEVI,*[a] SINDHU PRANAVI,[b] ROUSHAN NIGAM RAMNATH SHAW,[b] ESZTER MÁDAI,[a] DARSI JAYA PRASANNA KUMAR,[b] PRASAD GONUGUNTA,[a] PEYMAN TAHERI[a] AND ARJAN MOL[a]

[a] Materials Science and Engineering Department (MSE), Faculty of Mechanical Engineering (ME), Delft University of Technology, 2628 CD Delft, The Netherlands; [b] Department of Chemical Engineering, M.S. Ramaiah Institute of Technology, Bengaluru 560054, India
*Emails: P.RaviAnusuyadevi@tudelft.nl; ranu.prasaanth@gmail.com

1.1 Introduction

Excessive population growth coupled with rampant, irrational, and exploitative industrial practices has strained the environment. This generation demands inherently safe and eco-friendly engineering practices. The increase in global computing power has accelerated the search for exquisite high-tech materials to build a sustainable future. In due course, two-dimensional (2D) nanomaterials have gained momentum in the research world due to their exotic properties and various energy and environmentally oriented applications.

Nanoscience & Nanotechnology Series No. 66
Next-generation 2D Nanomaterials for Sustainable Energy and Environment-oriented Applications: Electrocatalysis, Photoelectrocatalysis and Photocatalysis
Edited by Narinder Singh and Ashish Kumar

Published by the Royal Society of Chemistry, www.rsc.org

2D nanomaterials are those materials that have at least one dimension on a 1–100 nanometre scale. This advanced class of materials can have lateral sizes going up to a micrometre, or larger, scale.[1] These are characterized by single- or few-layered structures with strong intralayer covalent bond interactions and weak van der Waals (vdW) forces between adjacent layers.

Compared to three-dimensional (3D) materials and their bulk counterparts, 2D nanomaterials exhibit several unique characteristics. First, confinement of electrons within two dimensions, especially in a single-layer nanosheet, results in compelling electronic properties that are absent in other nanomaterials, making them promising for various applications.[2] Furthermore, these properties are tuneable through modification of the synthetic methodologies, making them versatile. Second, their atomic thickness, along with covalent bonding, provides maximum mechanical flexibility and optical transparency bonding.[3]

Furthermore, the large lateral size and atomic thickness of ultrathin 2D materials results in very high specific surface areas and increased ratios of exposed surface atoms, making them supremely suitable for energy storage and engineering applications, such as for catalysis, supercapacitors, spintronics, valleytronics, *etc.* Their specific surface area also makes them promising as building blocks for functional composites, acting as templates for synthesizing other nanostructures, or as reinforced fillers to strengthen composite materials.[4]

Interest in 2D nanomaterials has surged since Novoselov, Geim, and their team isolated graphene from graphite in 2004.[5] Graphene, a single-atom-thick carbon film, boasts remarkable properties, such as high carrier mobility, large surface area, good optical transparency, high Young's modulus, and excellent thermal/electrical conductivity. This discovery sparked exploration into similar materials, such as transition metal dichalcogenides (TMDs), MXenes, transition metal oxides (TMOs), hexagonal boron nitride (h-BN), metal–organic frameworks (MOFs), black phosphorus, and many others materials (expanding the range of 2D nanomaterials), especially due to their alluring interchangeable electronic properties (see Figure 1.1). Various fabrication methods, from mechanical cleavage and chemical synthesis to chemical vapor deposition (CVD) and pulsed layer deposition (PLD), have been developed.[6] This chapter gives a brief overview of the properties, synthesis techniques, and applications of a few emerging high-tech 2D nanomaterials, namely, graphene, reduced graphene oxide (rGO), graphene oxide (GO), graphitic carbon nitride (g-C_3N_4), TMDs, MXenes, TMOs, and hexagonal boron nitride in the following sections.

1.2 Graphene

Graphene, a two-dimensional (2D) material, is an allotrope of carbon in which a single layer of carbon atoms is arranged in a honeycomb lattice structure.[7] In its planar structure, the carbon atoms are sp^2 hybridized, with a carbon bond length of 0.142 nm. Individual layers of graphene are stacked

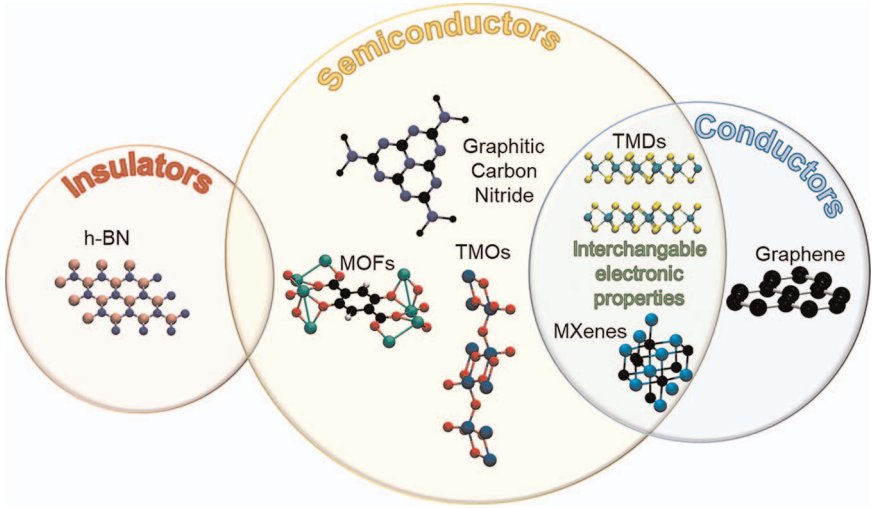

Figure 1.1 Schematic representation of some notable layered 2D nanomaterials researched intensively for their intriguing properties and potentially valuable applications, especially addressed for their interchangeable electronic properties depending on the synthesis conditions. These materials, their properties and recently updated synthetic methodologies are systematically addressed in this chapter.

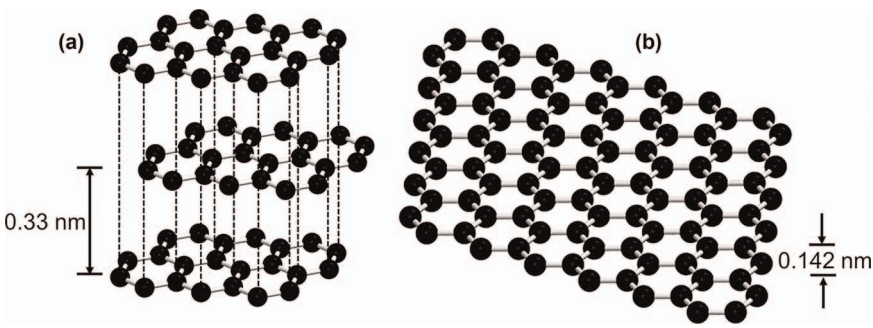

Figure 1.2 (a) Graphite, an allotrope of carbon, made up of multiple monolayers of graphene, held together by weak van der Waals (vdW) forces with an interlayer distance of 0.33 nm. (b) Single layer of carbon atoms arranged in a hexagonal lattice forming the graphene monolayer with a thickness of 0.35 nm, where the bond length between carbon atoms is 0.142 nm.

to form graphite, with an interlayer spacing of 0.33 nm (see Figure 1.2), held together by vdW attraction forces. Owing to the weak forces between the layers of graphene in the bulk graphite, they can be easily exfoliated into individual monolayer graphene sheets of thickness 0.35 nm.[8]

1.2.1 Properties of Graphene

Graphene is a zero-bandgap material and the strength of defect-free graphene is 300 times stronger than that of steel.[9] It exhibits a high surface area of 2630 $m^2 g^{-1}$ and very high electron mobility of 15 000 $cm^2 V^{-1} s^{-1}$.[10] Its exceptional thermal conductivity reaches 5300 $W m^{-1} K^{-1}$ at room temperature, which is ten times higher than that of copper,[11] 100 times higher than silicon, and 5000 times that of graphite.[10] This high thermal conductivity is attributed to the continuous π-orbital formed by electron clouds on both sides of the carbon ring (see Figure 1.3), enabling facile movement of electrons throughout the graphene structures.[12] A single layer of graphene absorbs only 2.3% of the incident light, and 97.7% of light passes through the layer, making it a viable candidate for designing transparent electrodes, touch screens, solar cells, and light-emitting diodes.[13] It is a hydrophobic material and forms agglomerates in aqueous media. Defect-free crystalline graphene is stable and exhibits inertness, due to stable bonding between carbon atoms, and does not undergo any chemical reactions under normal conditions.[14]

1.2.2 Synthesis of Graphene

Graphene synthesis is broadly classified into top-down and bottom-up approaches.[15] In the top-down approaches, the individual graphene nanosheets are derived from bulk parent material, usually graphite. Commonly used techniques to synthesize graphene by a top-down approach are mechanical exfoliation,[16] liquid-phase exfoliation,[17] chemical exfoliation,[18] microwave techniques,[19] axial unfurling of nanotubes,[19–21] and graphene oxide reduction[22–25] (see Figure 1.4). The bottom-up approach uses carbon atoms as building blocks, and the techniques in this category are CVD[26] and epitaxial methods.[27]

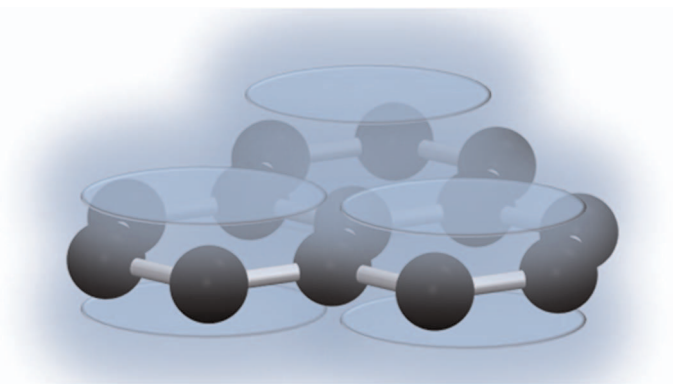

Figure 1.3 Schematic depiction of electron clouds on both sides of the carbon ring due to the continuous π-orbitals.

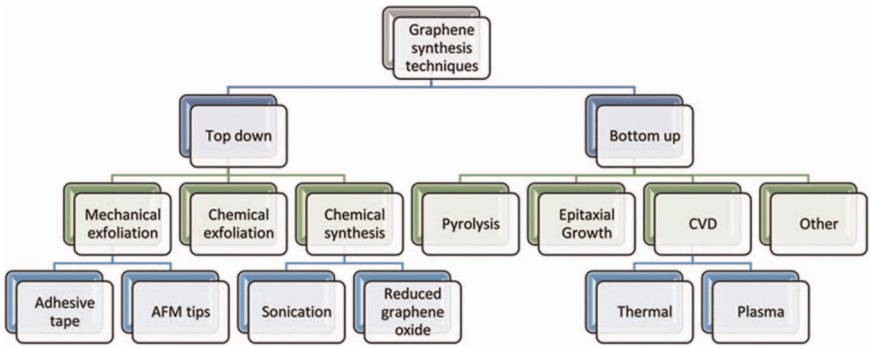

Figure 1.4 The various synthetic strategies for producing 2D graphene nanosheets.[38] Reproduced from ref. 38, https://doi.org/10.1007/s40089-015-0176-1, under the terms of the CC BY 4.0 license, https://creativecommons.org/licenses/by/4.0/.

1.2.2.1 Mechanical Exfoliation

Mechanical exfoliation is a technique in which graphene layers are moved from graphite to an adhesive material, such as Scotch tape. The tape is gently stuck onto the surface of the graphite to peel graphene by shear action.[28] The weak interlayer forces and large layer spacing in the perpendicular direction enable exfoliation of individual layers.[29] Novoselov and Geim harnessed this technique to make graphene for the first time.[16] This method is efficient in producing monolayers of graphene with good structural properties and electronic configurations. The major drawbacks of this method, which render it inefficient, are the relatively low yields and long production times.[30]

1.2.2.2 Liquid-phase Exfoliation

Liquid-phase exfoliation (LPE) is a three-step process involving dispersion of graphite in a solvent, exfoliation, and purification. The exfoliation process involves two subprocess: sonication and shear force application in a high-shear mixer. Sonication disperses graphite flakes in a solvent and subjects them to sound waves, generating cavitating bubbles that implode, producing shockwaves and microjets.[31] Shear mixers generate intense shear forces to exfoliate the graphite.[32] Suitable solvents are essential for stable graphene dispersions. The efficiency of LPE relies on the sound wave intensity, solvent type, and centrifugation conditions, where centrifugation removes bulk aggregates to isolate few-layer and monolayer graphene.[33]

1.2.2.3 Chemical Exfoliation

Direct top-down fabrication of graphene monolayers from bulk graphite involves lower yields, in contrast to chemical exfoliation, which enables

higher yields compared to the above methods. However, this technique involves generation of graphene oxide, from which graphene-related materials are derived. Graphene oxide is produced by the Brodie, Hummers, and Staudenmaier methods.[34,35] The commonly used Hummers method employs strong oxidizing agents, such as H_2SO_4, $KMnO_4$, and $NaNO_3$, to oxidize graphite to produce graphitic oxide.[34] Here, the interlayer spacing between the layers of graphene is increased by forming graphene-intercalated compounds (GICs).[36] Then, using sonication or heating, GICs are exfoliated into single- to few-layer GO nanosheets. The resulting GO contains dense oxygen functional groups, such as hydroxyl, epoxy, and carboxylic acid moieties. It must be reduced to attain graphene-related characteristics.[37] Such reduction can be achieved using agents such as hydrazine, hydroxylamine, glucose, ascorbic acid, hydroquinone, alkaline solutions, sodium borohydride, and pyrrole.[38]

1.2.2.4 Chemical Vapor Deposition

The synthesis of graphene through CVD processing involves the thermal decomposition of gaseous precursors containing carbon molecules at higher temperature (~1000 °C) and their subsequent deposition onto the substrate surface.[39] The decomposed carbon species diffuse on the substrate surface and arrange themselves into graphene layers. Precursors, such as methane, ethylene, acetylene, ethanol, and benzene, are decomposed on various transition metal substrates, such as Ni, Pd, Ru, Ir, and Cu.[26] Graphene was first synthesized, in 2006, using a camphor ($C_{10}H_{16}O$) precursor on Ni foil.[38] CVD produces graphene monolayers with large lateral dimensions, thereby rendering it a viable candidate for several electronic and energy devices.[40] This method ensures large-area films, control of thickness of the nanosheets, and its adaptability with various substrates. However, post-separation of the graphene monolayers from the substrate is still not a trivial task.[41]

1.2.2.5 Epitaxial Growth

In this method, graphene is formed over a crystalline substrate, where the fabricated 2D nanosheets possess crystalline features that are the same as the substrate material. The resultant layer is commonly known as the epitaxial layer.[42] Here a smooth and contaminant-free surface with a hexagonal lattice structure is frequently used as a substrate for graphene formation. For example, silicon carbide (SiC) provides a natural pattern (template) for graphene formation owing to its similar lattice structure. To obtain graphene, precursor gas is passed over the substrate in a controlled environment in the temperature range 1100–1600 °C.[42] Epitaxial graphene formation on SiC has been recognized as a viable route for mass production of graphene for electronic devices. Examples include high-frequency electronics, light-emitting devices, and radiation-resistant devices.[43] This technique ensures high-quality single-layer graphene with desirable properties

for its applications in electronic and optical devices. Nevertheless, this method demands specialized equipment and accurate growth conditions. Therefore, it is considered more challenging and expensive compared to other techniques, such as CVD.

1.3 Graphene Oxide and Reduced Graphene Oxide

Graphene's poor solubility and production issues associated with large-scale synthesis at lengthier lateral dimensions make it challenging to unlock its engineering application potential.[44,45] As a substitute, an analogous structure of graphene can be synthesized by a top-down approach using graphite as a parent material. Here, graphite is exfoliated using oxidizing agents in the presence of suitable solvents to yield graphite oxide, comprising several monolayers of graphene oxide. Each of these layers of GO material comprise myriads of oxygen functional groups. GO is easily dispersed in many solvents, processed, and functionalized, thereby rendering it well suited as a precursor for graphene.[46,47] GO is an insulating material owing to the presence of oxy functional groups, such as hydroxyl and epoxy groups at its basal plane and edges.[48] The GO can be made conductive by reducing these oxy functional groups with a variety of techniques, resulting rGO. A systematic methodology for obtaining GO and rGO from graphite is shown in Figure 1.5. Graphene-like properties render rGO a highly desirable material to be used in a spectrum of applications, such as in sensors,

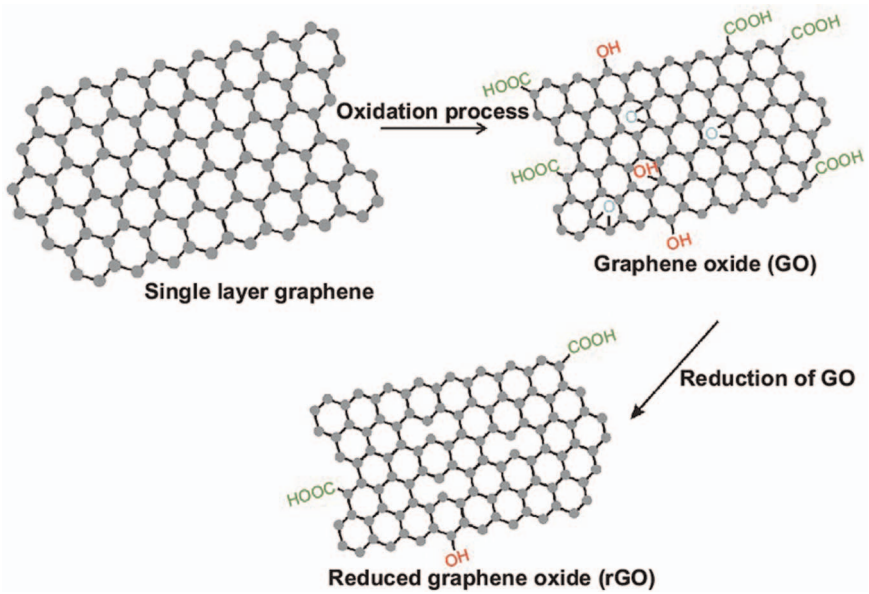

Figure 1.5 Synthesis of rGO and GO from graphene, derived from the graphitic material.[292] Reproduced from ref. 292 with permission from Elsevier, Copyright 2018.

biomedical, environmental, and catalytic applications, as well as in optoelectronic and storage devices.[49–51]

1.3.1 Properties of GO and rGO

1.3.1.1 Mechanical Properties

GO produced by a modified Hummers' method has shown an elastic modulus value near to that of graphene.[52] GO successfully serves as a filler for increasing the tensile strength of polymers. For example, 20% GO filler in polyvinyl alcohol (PVA) has been shown to result in an enhanced tensile strength of five times that of the pure PVA film.[53] The marked increase in the mechanical properties of the composite are a result of the high degree of bonding between the PVA and the oxy functional groups of the GO. In a similar study, 0.1 wt% of GO in polyurethane (PU), used in the vulcanizing process of rubber, increased the tensile strength by 16.4%.[54] It has also been reported that GO decorated with ruthenium and cerium nanoparticles (0D–2D) results in enhanced catalytic activity for the oscillatory Belousov–Zhabotinsky reaction.[55–57]

1.3.1.2 Electric Properties

Electrically conductive polymers are developed by incorporating rGO as a filler.[58] GO is a semiconductor due to abundant oxy functional groups and disruption in sp^2 hybridization, and can be made conductive by reducing the functional groups using established techniques.[59] It has been corroborated that the conductivity is increased by several orders of magnitude after reduction, but less than that of pristine graphene. This difference is due to traces of oxygen bonded to carbon, which disrupts the charge carriers and occurrence of electron transport through a hopping mechanism. Researchers have shown that GO reduced in the presence of hydrazine hydrate improved the conductivity by five orders of magnitude. Similarly, reduction of GO using a conventional microwave operated at 1000 W for 1–2 s has shown improved electron mobility, from 0.0001 to 0.1 $m^2 V^{-1} s^{-1}$, in field-effect transistors.[60] Other techniques to reduce GO are treatment with HI and KOH.[61,62] With 24 wt% of rGO as a filler in a polyaniline (PANI) polymer composite, it functions as a flexible supercapacitor and displays a conductivity of 9.06×10^4 $S m^{-1}$.[63] The improved conductivity is attributed to compact packing of PANI with rGO.

1.3.1.3 Thermal Properties

Graphene has a very high thermal conductivity, in the range 3000–5000 $W m^{-1} K^{-1}$, whereas GO has very low thermal conductivity, of 0.5–1 $W m^{-1} K^{-1}$. It is very important to reduce GO to rGO so that its application can be realized in materials that require good thermal

properties.[64] The thermal conductivities of polymer systems, such as epoxy and styrene butadiene rubber, are improved upon incorporating rGO.[65] Likewise, the addition of 27.2 wt% of rGO in poly(vinylidene fluoride-*co*-hexafluoropropylene) has shown a thermal conductivity of 19.5 $W m^{-1} K^{-1}$.[66] The conductivity of rGO lies in between that of GO and graphene. The mechanical properties are near those of graphene and it is used in composite materials to enhance the flexibility and strength. rGO is chemically more stable compared to GO, owing to the removal of oxy functional groups during reduction. The thermal stability of rGO is very high (~750 °C), enabling its implementation in high-temperature applications.[67]

1.3.2 Synthesis of GO and rGO

GO is synthesized *via* a top-down approach, by oxidizing graphite with strong oxidizing agents.[34,35] This yields graphite oxide, with oxygen groups intercalated between graphite layers. Sonication separates the layers into mono- to few-layer GO nanosheets. rGO derived from GO through reduction often has defects.[68] Ascorbic acid offers a green alternative, providing efficient reduction without the use of toxic agents, such as hydrazine hydrate.[69]

1.4 Graphitic Carbon Nitride

The class of polymeric materials composed of carbon and nitrogen are known as carbon nitrides. Among this class, graphitic carbon nitride (g-C_3N_4), a non-metallic semiconductor,[70] has received significant research interest in the areas of energy conversion, photocatalysis, hydrogen production, *etc.*[71–74] It is the most stable allotrope of carbon nitride under ambient atmosphere and its surface is basic in nature.[75,76] The g-C_3N_4 portrays a graphene-like 2D structure and is made up of s-triazine units. This building block of g-C_3N_4 is shown in Figure 1.6. It has a bandgap of 2.7 eV, thereby rendering it an effective visible light photocatalyst.[77,78] The functional groups NH_2 and NH present at the edges serve as crucial sites for conversion, active catalysation, and CO_2 activation.[78] It exhibits several exceptional characteristics, such as a moderate and tuneable bandgap, chemical and thermal stability, high surface area, and ease of synthesis.[79] These materials were primarily investigated for their photocatalytic abilities, and they have emerged as viable materials for diverse engineering applications, including catalysis, sensing, bioimaging, and in the energy sector.[80–82]

1.4.1 Properties of g-C_3N_4 Materials

The thermal stability of g-C_3N_4 is the highest among many organic materials. It starts undergoing thermal decomposition at a temperature higher than 600–700 °C, and completely decomposes at 750 °C.[83] The choice of synthesis

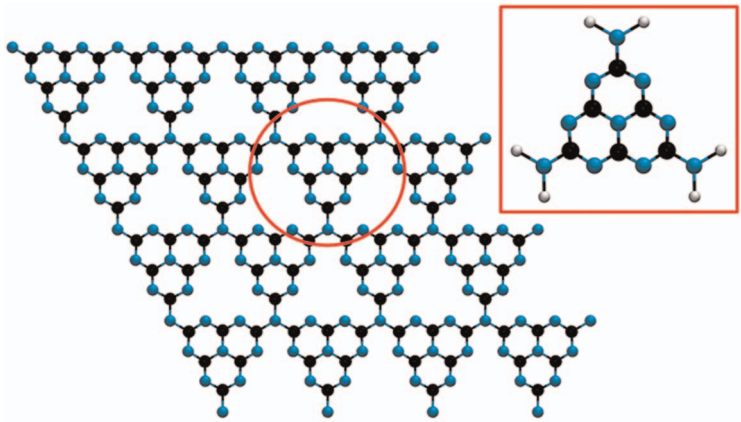

Figure 1.6 Schematic depiction of triazine building unit forming the g-C_3N_4 nanosheet (blue: N, black: C, white: H).

method and precursors dictates the stability of the g-C_3N_4.[79] The high thermal stability of g-C_3N_4 enables its use in various applications: for example, as a heterogeneous organic catalyst, at an operating temperature below 500 °C.[79] In addition, these materials also exhibit very good chemical stability: they do not degrade in water, acid, and many organic solvents.[84] Treating bulk g-C_3N_4 with acids will exfoliate it into individual sheets without destroying its base planar structure.[85]

For efficient photocatalytic water splitting, the photocatalyst bandgap energy should ideally fall between 1.23 eV and 3 eV, allowing utilization of the visible light spectrum to provide sufficient energy for the process. Effective photocatalysts in the literature typically exhibit bandgaps larger than 2 eV. g-C_3N_4, with a bandgap energy of 2.7 eV has demonstrated efficient visible light photocatalytic water splitting in the presence of sacrificial donors.[86] Notably, a self-propelling photocatalytic system was fabricated recently using a g-C_3N_4 semiconductor material.[87]

1.4.2 Preparation of g-C_3N_4 Materials

To ensure practical engineering applications, g-C_3N_4 must have well-controlled mono- to few-layered thickness and porous structures.

1.4.2.1 Hard- and Soft-template Method

Templating involves replicating a structure into another through structural inversion, and is a versatile technique for preparing nanostructured porous materials.[88] Hard templates, such as silica nanospheres[89] or SBA-15,[90] are utilized for creating porous g-C_3N_4 architectures with tuneable pore diameters. This method ensures high specific areas and open pores, but requires environmentally harmful template removal processes using NH_4HF_2 or

HF.[79] By contrast, soft templates, such as amphiphilic surfactant molecules, offer a greener approach, with template removal achievable through calcination.[91] Different morphologies and specific surface areas of g-C_3N_4 can be achieved using various surfactants or liquids as soft templates, as exemplified by mesoporous g-C_3N_4 fabricated with Triton X-100.[92]

1.4.2.2 Template-free Method

Porous g-C_3N_4 can also be obtained by facile thermal treatment of a dicyandiamide precursor. The thus-prepared porous g-C_3N_4 has shown a high Brunauer–Emmett–Teller (BET) surface area (201–209 $m^2 g^{-1}$) and large pore volume (0.50–0.52 $m^3 g^{-1}$).[93] Graphene-modified porous g-C_3N_4 (porous g-C_3N_4/graphene) was also synthesized by thermal calcination.[94]

1.4.2.3 Exfoliation of Bulk g-C_3N_4

Bulk g-C_3N_4 powder can be produced by polycondensation of affordable nitrogen-containing organic precursors, such as urea, thiourea, melamine, cyanamide, dicyandiamide, and guanidine hydrochloride. Despite its 2D layered structure, akin to graphene, bulk g-C_3N_4 typically has a low specific surface area (usually below 20 $m^2 g^{-1}$). Inspired by graphene's exfoliation from graphite, the delamination of bulk g-C_3N_4 into mono-/few layers of g-C_3N_4 is seen as an effective approach to increase the specific surface area, given that the theoretical specific surface area of ideal monolayer g-C_3N_4 can reach as high as 2500 $m^2 g^{-1}$.[95]

1.4.3 Conclusion for Graphene/GO/g-C_3N_4

The exceptional electronic and electron transport characteristics of graphene suggest its potential as a substitute for silicon in future electronics and optoelectronics. However, its lack of a bandgap, which is linked to Dirac fermions, inhibits its suitability for these applications.[96] Additionally, graphene sheets tend to aggregate or form stacks due to interlayer vdW forces, which are particularly evident in aqueous solutions. This aggregation impedes the dispersion of graphene in composites and solutions, thereby diminishing its efficacy in applications such as coatings, composites, and in energy devices, such as supercapacitors and hydrogels, where porous structures are desired.[97]

Even though defect-free graphene represents an ideal material for various applications, yet current fabrication methods remain immature. Atomic layer deposition (ALD) encounters difficulties when applied to graphene because of the absence of reactive surface sites. Consequently, this results in the preferential growth of grain boundaries, wrinkles, and defects within the graphene structure (a non-uniform sheet is formed).[98] Furthermore, scaling up the production of graphene-based materials at an economically viable cost remains highly challenging. The production of monolayer graphene

with high purity remains a formidable challenge, thereby constraining the scalable manufacturing of graphene and its prospective commercial applications. Essentially, a comprehensive assessment of the potential health hazards associated with graphene-based materials is imperative before considering widespread utilization on a large scale. For instance, the use of hazardous chemicals, such as hydrazine, borohydrides, and aluminium hydride, as reducing agents in the oxidative exfoliation-reduction method has restricted its commercialization due to potential environmental risks.[99] Despite the enhanced performance of exfoliated g-C_3N_4 sheets, compared to its bulk counterpart, its real-world implementation is hindered due to complexities associated with the large-scale synthesis of these nanostructured materials.[100]

All these drawbacks of graphene-based 2D materials have prompted research and development of many other materials, such as TMOs, TMDs, MXenes, h-BN, *etc.*, which offer a plethora of properties that can be tailored according to the application required. The properties, synthesis, and applications of these are elucidated in the following sections of this chapter.

1.5 Transition Metal Dichalcogenides

The TMDs represent a group of 2D layered materials that exhibit behaviour differing from that of graphene. In contrast to graphene's single atomic carbon thick layer, TMDs are composed of a transition metal array sandwiched between two similar/dissimilar chalcogen arrays (S, Se, or Te). Hence, the materials within the realm of TMDs can be designated/abbreviated as MX_2 (M = transition metal and X = S or Se or Te). Within each unit or individual layer, there are three different atomic planes (here, the top and bottom chalcogen layer could be either the same or different, depending on the material) positioned along the lateral direction. The quintessential atomic bonding in these layered TMDs happens in such a way that each metal atom requires two chalcogen atoms, so that the oxidation states are +4 for the metal and −4 for the two chalcogen atoms combined.[101]

Each monolayer/slab of TMD material is composed of three sublayers of atomic planes (X–M–X). Here, the transition metal atom sublayer is bonded covalently to the chalcogen sublayer, above and below it, whereas each monolayer within the bulk architecture of the TMD is bonded with each other through vdW forces. These TMDs display different polymorphs (different crystalline structures) due to their typical diverse polytypes (diverse stacking of atomic planes within a monolayer).[102] As these monolayers are held together by weaker interactions between the interlayers, they can easily be exfoliated by a myriad of top-down approaches, resulting in the synthesis of monolayers of TMDs.

The conventionally observed crystalline phases in the family of TMDs can be classified into two fundamental types: the H phase and the T phase. There are two different polytypes present within the H phase system and these are designated as 2H and 3R phases. Here, the letter 'H' refers to a hexagonal

and 'R' to a rhombohedral structural arrangement, and the integer prefixing these letters indicates the number of monolayers present in the unit cell of the crystalline structure. Specifically, in the 2H phase, the chalcogen atoms present in the different atomic planes within the monolayer are horizontally located in the same position, but vertically perpendicular to the direction of the atomic plane they are positioned on top of each other, thus following the 'AbA–BaB' stacking configuration.

Here, the capital letters A and B denote the chalcogen atoms and the small letters b and a denote the transition metal atoms (see side view portion in Figure 1.7a). In the case of TMDs with a 3R phase, the position of the chalcogen atom within each monolayer follows the same pattern as the 2H phase, however, their stacking configurations follow the sequence 'AbA–CaC–BaB', which is systematically depicted in Figure 1.7b.

These two diverse polytypes (2H and 3R) within the H-phase crystal system follow the same metal coordination: each transition metal atom coordinates with the surrounding six neighbouring chalcogen atoms and the branching is such that it forms a trigonal prismatic (D_{3h} group) geometry composed of two tetrahedrons. In this structure, the metal is positioned in the centre point (symmetry point) and three branches of chalcogen atoms are on the upper tetrahedron and the remaining three in the bottom tetrahedron (see Figure 1.7a). This results in a 2D honeycomb lattice with hexagonal symmetry, when the 2H phase is seen in top view, as shown in Figure 1.7a. Irrespective of the trigonal prismatic metal coordination in the 3R polytype, the stacking pattern exhibits an in-plane shift with respect to the first layer, resulting in a staggered disposition.[103] Importantly, an auxiliary atom is present exactly in the centre of the honeycomb lattice,[104] as observed in the top view of the structure (see Figure 1.7b).

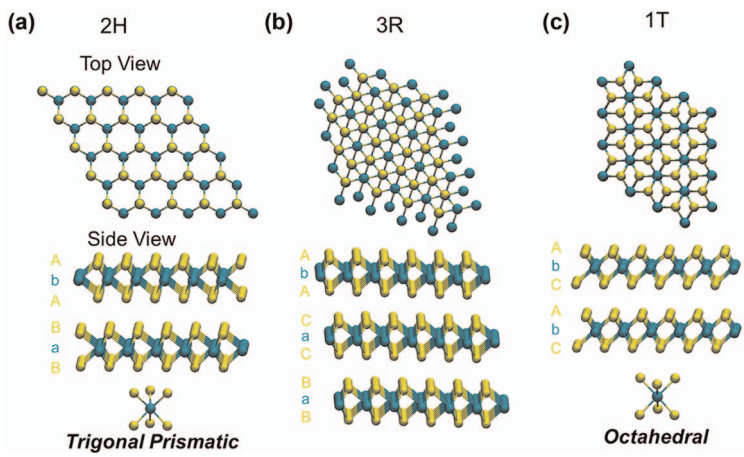

Figure 1.7 Schematic representation of various polytypes present in the family of transition metal dichalcogenides: (a) 2H phase, (b) 3R phase, and (c) 1T phase.

Finally, the remaining polymorph present in the family of 2D TMDs is the T-phase crystal system. Here, the chalcogen atoms within the monolayer in different atomic planes occupy different positions and are not located on top of each other, resulting in an 'AbC' stacking configuration (see Figure 1.7c). In the T-phase crystal structure, the metal atom coordinates by branching with the surrounding six chalcogen atoms and forms an octahedral structure (D_{3d} group). Such a structure is formed with a transition metal atom in the centre and three chalcogen atoms branching to this metal atom trigonal prismatically, forming a tetrahedron structure on the top, and the other tetrahedron (trigonal antiprism) structure in the bottom is obtained by rotating the top tetrahedron by 180° (see Figure 1.7c). This eventually results in a hexagonal arrangement of the chalcogen atoms, when observed in the top view (see Figure 1.7c) and this polytype is termed the 1T phase (D_{3d} point group). Apart from the 1T-octahedral structure, the other polytypes present in the T phase system are 1T′ and $1T_d$ phases. The 1T′ phase is obtained through the distortion of the octahedral structure in the conventional 1T phase. This happens when the 1T phase is unstable and the crystal structure relaxes through the dimerization of metal–metal bonds[105] (see Figure 1.8a). In certain members of the TMD family ($MoTe_2$, WTe_2, *etc.*), the distortion of the 1T phase results in orthorhombic metal coordination,[104,106] resulting in the formation of the $1T_d$ polytype within the T-phase crystal system (see Figure 1.8b). Thus, in accordance with the stacking configurations of the atomic sublayered planes within a monolayer, the TMDs form different polytypes and, based on the metal coordination with adjoining chalcogen atoms, various polymorphs of TMDs are formed. To conclude, the monolayer of TMDs exhibit rudimentarily either the H-phase (trigonal prismatic coordination) or T-phase (octahedral) crystal structure.

Based on the constitution of TMDs, with transition metal (group 4, 5, 6, 7, 8, 9, or 10) and chalcogen (S, Se, or Te) components, the thermodynamically stable crystal structure is either 2H or 1T phase, while other polymorphs exist in the metastable state. The favoured stable phase with the lowest energy displayed by the TMD material is predominantly determined by the

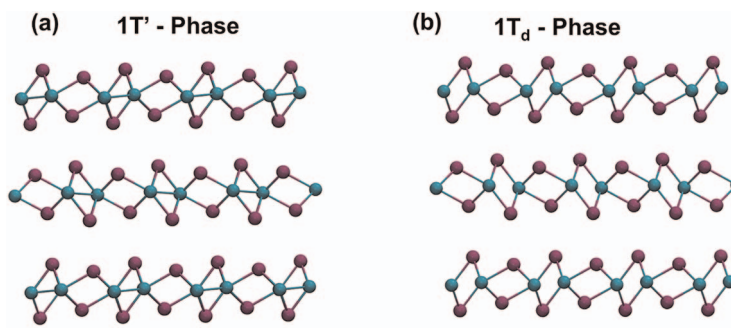

Figure 1.8 The primarily observed distorted 1T phases: (a) 1T′ phase and (b) $1T_d$ phase in TMD materials.

transition metal atom, and, specifically, by the number of d electrons possessed by the transition metal in the particular transition metal dichalcogenide. On the other hand, TMDs with group 6 transition metals (d^2 configurations, that is, a d electron count of 2) display an H-phase crystal structure with trigonal prismatic coordination. Group 5-based TMDs (d^1 configurations) exhibit both H-phase and T-phase crystal structures. Finally, TMDs with group 7 metals (d^3 configurations) are conventionally observed with the distorted octahedral crystal structure (T′ phase).[101,106]

1.5.1 Electronic Structure and Properties of 2D TMDs

The rudimentary electronic characteristics of 2D TMDs can be perceived from the ligand field splitting and the number of d electrons possessed by the transition metal in the TMD. The non-bonding d bands in the X–M–X bonds are composed of d orbitals of the transition metal and are positioned in the gap region between the antibonding (σ*) and bonding (σ) orbitals (bands) established by the X–M bonds (see Figure 1.9). In TMDs with trigonal prismatic coordination (H phase system), the ligand field splitting of the d orbitals of the transition metals forms three specific bands: $a'_1(d_{z^2})$, $e'(d_{x^2-y^2, xy})$, and e″ $(d_{xy, yz})$, which are separated by a distinct energy gap:[107] see the progressive filling of d orbitals for groups 5 and 6 in the bandgap in Figure 1.9. On the other hand, TMDs with octahedral coordination (T phase system) form two degenerate orbitals: $t_{2g}(d_{xy, yz, zx})$ and $e_g(d_{x^2-y^2, z^2})$[101,108] (see band diagrams for groups 4, 7, and 10 in Figure 1.9). The myriad electronic properties of TMD materials arise from the number of electrons occupying the non-bonding transition metal d orbitals, or, in simple terms, the electronic behaviour is dependent on the d electron count of the transition metal atom in the TMD, as this count directly influences the location of the Fermi energy level (E_F).

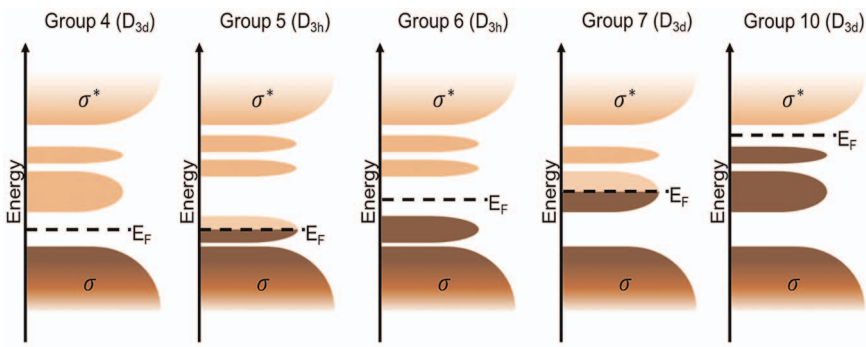

Figure 1.9 Schematic depiction of energy levels in TMD materials composed of transition metals from groups 4, 5, 6, 7, and 10, illustrating the progressive filling of the various d bands located within the region of bonding (σ) and antibonding (σ*) states.[101] Adapted from ref. 101 with permission from Springer Nature, Copyright 2013.

When these non-bonding orbitals are not filled, as in the case of group 4 TMDs, or are completely filled with six d electrons, as for group 10 TMDs,[101,109] the E_F is positioned within the energy gap between the orbitals, leading to semiconducting behaviour. When the d_{z^2} and $d_{xy,\,yz,\,zx}$ orbitals are partially filled, as in the case of group 5 and 7 TMDs, respectively, then the resultant Fermi level is positioned within the partially occupied d orbitals, where these TMDs exhibit metallic character in their electronic properties: for example, in 2H-$NbSe_2$ and 1T-ReS_2[101] with group 5 and 7 band schematics as shown in Figure 1.9. The two d electrons in group 6 TMDs completely fill the a_1' (d_{z^2} orbitals) bands[107,109] (see Figure 1.9) thus making the 2H-MoS_2 exhibit semiconducting behaviour. Interestingly, the stable 2H phase of group 6-based TMDs can be transformed into the T phase (octahedral coordination) by intercalating the material with alkali metals (lithium, sodium, and potassium intercalation[110,111]) or by exposing the TMD material to a high-dose electron beam, where a 2H→1T transformation is achieved through intralayer atomic plane gliding.[112]

The former technique of ion intercalation is the conventional strategy employed in TMDs for phase engineering. Here, the original stable phase is destabilized by the effective change of the d electron count, through donation of the electron from the valence s orbital of the alkali metal to the d orbital of the transition metal. Such redistribution of d orbitals in group 6 TMDs, results in transformation to T-phase crystal structure, which eventually results in the partial filling of the t_{2g} orbital (see Figure 1.10), and thus the phase transformation through ion intercalation in group 6 TMDs results in electronic characteristics with metallic behaviour. Apart from the influence of the d electron count of the transition metal atom on the electronic structure of the TMD, the electron count of the chalcogen

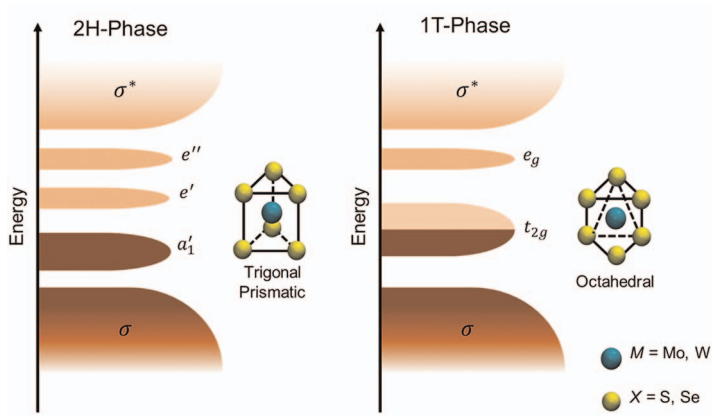

Figure 1.10 Schematic illustration of the density of states for group 6-based TMDs and the corresponding conversion to the 1T phase upon intercalation or through any other external driving force.[101] Adapted from ref. 101 with permission from Springer Nature, Copyright 2013.

atom also displays an altering trend. With the increase in the electron count (atomic number) of the chalcogen atom, there is a scaling decrease in the bandgap of the semiconductor material within the family of TMDs. For example, when the chalcogen atom was changed from S to Te in group 6 TMDs ($MoS_2 \rightarrow MoSe_2 \rightarrow MoTe_2$), the experimentally observed indirect bandgap was 1.37 eV for MoS_2, 1.25 eV for $MoSe_2$, and 0.89 eV for $MoTe_2$.[113] Such a decrease in the bandgap is due to the increase in the valence band (VB) edge, resulting in uplift of the VB minimum level, due to augmentation of the overlap of p–d orbitals with increasing atomic number of the chalcogen atom.[109,114] Subsequently, the conduction band offset is negligible, indicating that the influence of the chalcogen atom on the electronic structure is not as dramatic as that of the transition metal atom.[114]

1.5.2 Correlation Between Monolayer Count and Band Structure of TMDs

The group 6 TMDs, especially the molybdenum- and tungsten-based dichalcogenides are the most researched materials among the entire family of TMDs.[109] Most notably, MoS_2, $MoSe_2$, $MoTe_2$, WS_2, and WSe_2 are sufficiently stable under ambient conditions, rendering them ideal 2D materials for the sensitive detection of gaseous molecules.[115] Interestingly, for the same chalcogen atom, molybdenum is more reactive than the tungsten atom, due to the intrinsic higher reactivity of 3d electrons compared to 4d electrons. Thus, a larger atomic radius and reduced (diminished) reactivity reduce interaction between the transition metal and chalcogen atoms in TMDs. As a result, the stability of Mo-based TMDs is much higher than that of W-based TMDs.[109,116] Coupled with their stability and fascinating catalytic activity, Mo-based TMDs have found applications in sustainable renewable energy conversion, storage, and environmental related applications, for example: (1) 2H-MoS_2 serves as a visible light photocatalyst for treatment of pollutants and microorganisms;[117] (2) MoS_2- and $MoSe_2$-based heterolayers are employed as effective electrocatalysts for the HER;[118] and (3) 1T-MoS_2 and 1T-$MoSe_2$ have been studied as efficient electrocatalysts for Li–O_2 batteries.[119–121] The properties for such exalted catalytic activities for Mo-based TMDs stem from the intriguing evolution of their band structure in response to decrease in the thickness of the material when they are constricted from multilayer to monolayer materials.

Monolayered 2D nanosheets of TMDs became easily accessible with the report of large-scale synthesis of monolayers of MoS_2, $MoSe_2$, $MoTe_2$, and $TaSe_2$ through the liquid exfoliation technique.[122] When a semiconducting bulk TMD, such as 2H-MoS_2 or any material in the group 6 TMDs, is synthesized as a single monolayer it exhibits an interesting band structure that differs from the bulk counterpart. The bulk MoS_2 possesses an indirect bandgap of 1.2 eV, whereas the monolayer of MoS_2 transforms into a direct

bandgap of 1.9 eV.[123] When bulk, or even multiple layered (2L, 4L, 6L, *etc.*), 2H-TMDs are produced, the resultant material displays a crystal inversion symmetry. Here, the inversion centre is present between the two layers of the TMDs (see Figure 1.11a). However, in case of a monolayer or any odd number of layers, the inversion symmetry is dramatically broken. This leads to asymmetric potentials in the proximity of the atoms.[124] The hexagonal arrangement results in the occurrence of inequivalent valleys with the same energy but different momenta (K and K′), alternating at the six corners of the first Brillouin zone of group 6-based TMDs with monolayers (see Figure 1.11b and c). Coupled with the broken inversion symmetry, spin–orbit coupling (SOC) causes splitting of the valence band at these valleys at the K and K′ points. The spin projections in the K point are spin-up in the upper valley and spin-down in the lower valley, mirroring the projection at K′ (see Figure 1.11c). This effect is predominant in the VB of the semiconductor TMD, and the observed spin splitting energy is 0.148, 0.183, 0.426, and 0.456 eV for the upper valence band of 2H-MoS_2, 2H-$MoSe_2$, 2H-WS_2, and 2H-WSe_2, respectively.[125] This trend enables us to understand that the spin–orbit coupling is a relativistic effect and its magnitude is enhanced for heavier atoms. However, such spin splitting is very weak for the conduction band of the above materials, and it is about an order of magnitude less than the splitting energy observed for the valence band.[126]

To summarize, for the intrinsic electronic properties of monolayers of semiconducting TMDs, the broken inversion symmetry enhances the spin–orbit coupling. As a result, the valence band at the inequivalent valleys with different momenta splits, with spin-up and spin-down electrons (Figure 1.11c). This fascinating property is called spin–valley coupling (SVC), which subsequently enables the optical selection rule on these valleys, which empowers us to selectively excite the K valley using right-handed circularly

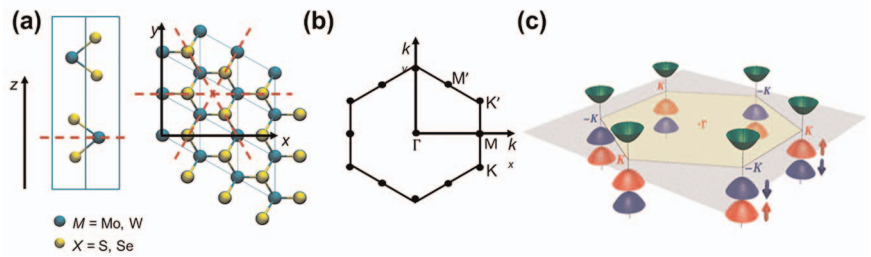

Figure 1.11 (a) Diagrammatic depiction of the side view and top view of the 2H-MoS_2 unit cell composed of two monolayers of MoS_2 material. (b) The first Brillouin zone of the MoS_2 monolayer.[125] (c). Band structure of MoS_2 with valence band splitting at K and K′(−K) points of the Brillouin zone.[127] (a) and (b) Adapted from ref. 125 with permission from American Physical Society, Copyright 2011; (c) reproduced from ref. 127 with permission from American Physical Society, Copyright 2012.

polarized light (σ+) with spin-up electrons and spin-down holes. Similarly, the K′ valley can be excited with left-handed circularly polarized light (σ−), generating excited spin-down electrons and spin-up holes[127] (see Figure 1.12a and b). This intrinsic SVC property energetically forbids the independent flipping of valley or spin, leading to an enhanced lifetime of the excited charge carriers.[128] These features enable the application of monolayered TMDs, such as MoS_2, in valleytronics devices, such as for quantum computing[129] and spintronics devices,[130] and also as an alternative cocatalyst in heterogeneous photocatalysis-based water splitting processes for hydrogen production.[131] Interestingly, concatenation of the above-mentioned monolayer MoS_2 with a chiral nematic cellulose-based film that selectively reflects left and/or right circularly polarized light, could pave the way for the fabrication of several smart devices in the future.[132–134]

Importantly, in the case of TMDs with an even number of monolayers (be it as a bilayer or as bulk material), the crystal inversion symmetry is not broken. This results in the strong suppression of the spin–orbit coupling, and subsequently there is no spin splitting at the inequivalent valleys at the K and K′ points of the Brillouin zone. These factors ultimately lead to decoupling of the spin and valley physics, under such a scenario, and when the TMD material is exposed to circularly polarized light, instead of selective excitation, both the inequivalent valleys are equally populated with net spin of electrons. This ultimately produces very weak photoluminescence in the TMD materials.

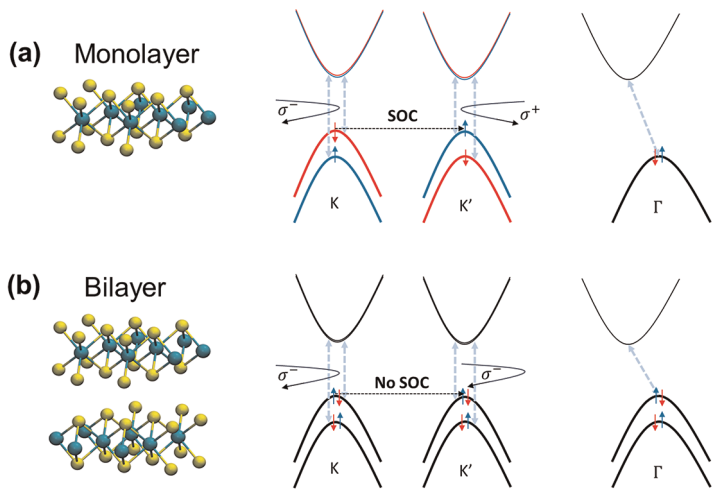

Figure 1.12 Diagrammatic representation of (a) monolayer and (b) bilayer present in 2H-phase TMD material along with the corresponding valence and conduction band levels. The enhanced spin splitting at the valence bands is due to spin–orbit coupling and the physics of the valley and spin are coupled in monolayers and not coupled in bilayers.[293] Adapted from ref. 293 with permission from the Royal Society of Chemistry.

Finally, the transition from indirect bandgap to direct bandgap semiconductor, when group 6 TMDs are exfoliated into a monolayered structure can be facilely elucidated by studying the electronic dispersion of the band structure. Figure 1.13 shows the density functional theory (DFT) calculations for bulk, several multilayers (8L, 6L, and 4L), and monolayers of MoS_2. In the case of bulk MoS_2, the indirect bandgap emerges from the valence band maximum at the Γ point and the conduction band minimum (CBM) at the Λ point (halfway between the K and Γ points of the Brillouin zone), as indicated by the slanting arrow between the blue (valence band) and green (conduction band) lines in Figure 1.13. Here, the valence band maximum at the Γ point is formed by the 2p orbitals of the sulfur atom, while the conduction band region at the K point is formed by the d orbitals of the molybdenum atoms. As the bulk TMD is exfoliated into a monolayer, there is a critical influence on the valence band maximum (VBM) at the Γ point as it falls below zero, and a new VBM is formed at the K point, resulting in direct transition from the VBM to CBM (direct bandgap) at the K point,[135] as indicated by a vertical arrow for the DFT of 2H-MoS_2 in Figure 1.13.

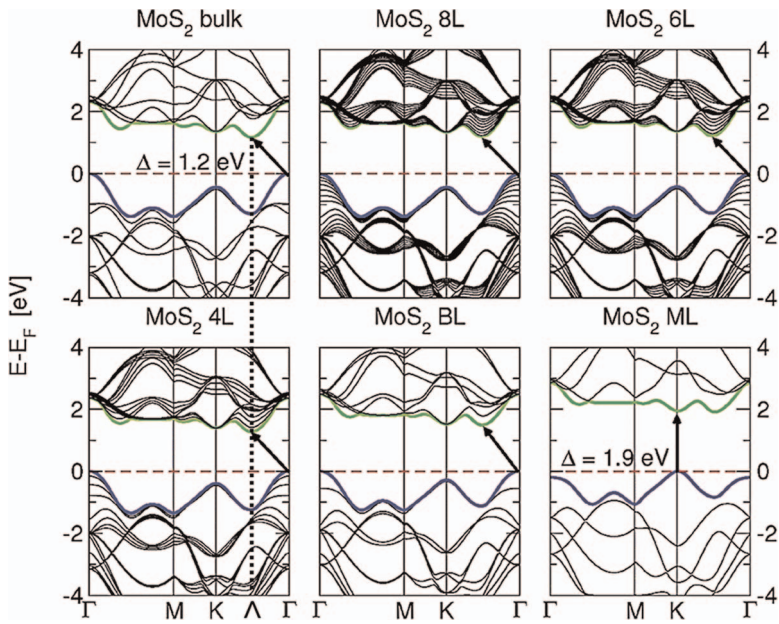

Figure 1.13 Band structure calculation of MoS_2 when exfoliated from bulk to monolayers. The dashed horizontal lines indicate the Fermi level and the calculations at the DFT/PBE level are without relativistic effects.[294] Reproduced from ref. 294 with permission American Physical Society, Copyright 2011.

1.5.3 General and Current Development in the Synthesis of 2D TMDs

The conventional top-down approaches for realizing monolayer TMDs are the Scotch tape-based mechanical exfoliation technique, wet chemistry-based solvent-phase exfoliation, and chemical intercalation strategies. The method in the first of these techniques is facile, involving peeling off of the multilayers of the TMD from the bulk crystal using Scotch tape and then subsequent deposition onto SiO_2/Si wafer substrates. However, this technique displays very low yield, and uncontrollability and uncertainty in the lateral size and number of monolayers, limiting its implementation in valuable applications.[136,137]

The wet chemistry-based chemical exfoliation technique not only provides us with the opportunity to achieve a large quantity of exfoliation from the bulk TMD material, but also enables structural modifications and doping of the layered 2D TMDs. The direct exfoliation in the liquid phase involves immersion of the bulk TMD in a solvent, followed by ultrasonication. The lateral size, thickness, uniformity, and properties (density of edge atoms exhibiting activity for catalysis) of the liquid-exfoliated nanosheets are heavily regulated by the solvent type, nature, and concentration of the parent bulk TMD material.[138,139] Importantly, the duration of ultrasonication also influences the dimensions of the resultant nanosheet and its properties. Prolonged sonication would eventually damage the structure of the exfoliated sheets, resulting in a high occurrence of defects, and preventing its implementation in electronic devices.[140,141] Finally, in the resultant suspension, stable dispersion of the nanosheets in the colloidal state is achieved through interaction between the solvent molecules and the nanosheets. As this interaction is of the vdW force type, the crystal phase of the bulk semiconductor TMD material (H phase) is retained successfully in the exfoliated nanosheets.[142]

Within the wet chemistry-based exfoliation strategy, the intercalation technique not only delivers facile production of nanosheets of TMDs, but also simultaneously induces a structural change in the resultant monolayers of the TMD material. Intercalation can be further divided into two types depending on the method used: (1) chemical intercalation and (2) electrochemical intercalation. Fundamentally, intercalation involves the injection of an ion (or molecule) into the space within the layered structured materials. Alkali metal ions (Li^+, Na^+, and K^+) are the commonly employed guest species for intercalation-based synthesis of 2D materials of TMDs (MoS_2, WS_2, WSe_2), other 2D families (such as h-BN), and graphite.[140,143] The bulk host material with such guest intercalants can be effortlessly exfoliated into nanosheets with internal (bubbling of gas) and/or external mechanical driving forces, such as sonication, thermal shocking, shearing, milling, *etc.*,[104,144,145] as the guest ion species weakens the vdW forces within the adjacent layers of the host material. The overall intercalation process involves the following steps: (1) the bulk parent material (MX_2) is first treated with the intercalating agent (for example, *n*-butyl lithium (C_4H_9Li) in hexane) to successfully produce an intercalated Li_yMX_2 compound and (2) this

inclusion complex (host + guest) Li_yMX_2 is reacted with water to yield H_2 gas, LiOH, and colloids of nanosheets of negatively charged TMDs.

To summarize this particular exfoliation process, the intercalation of alkali metal ions augments the interlayer spacing of the parent bulk material and reduces the vdW forces between the monolayers. The H_2 generated upon reaction of the inclusion complex with water drives the individual layers apart and the negative charge present on the nanosheets creates Coulombic repulsion and prevents aggregation.[142,146] The occurrence of such a negative charge is due to charge transfer from the valence electron of the lithium metal to the MX_2 layers. Such a charge transfer affects the atomic coordination of the 2H-TMDs, resulting in a crystalline phase transition from 2H (trigonal prismatic coordination) to 1T (octahedral coordination), and ultimately leading to the loss of semiconducting properties and the buildup of metallic properties. These fabricated 2D sheets with metallic properties find a tremendous number of applications in electrocatalytic activities involving hydrogen and oxygen evolution reactions.[142]

Notably, Goki Eda *et al.* fabricated a 2D monolayer of MoS_2, with a thickness in the range of 1–1.2 nm and lateral dimension of 300–800 nm, and, specifically in these nanosheets due to lithium intercalation in the MoS_2, 50% of the 1T (metallic) phase was observed.[147] Mohamed El Garah *et al.*[148] employed an electrochemical intercalation technique and synthesized mono-, bi-, and trilayers of MoS_2 comprising a lateral size of 800 nm and 40% 1T phase.[148] Sanghyeon Park *et al.*[149] used a molten (potassium) metal-assisted intercalation (MMI) approach coupled with mild sonication and successfully produced MoS_2 nanosheets of 1–3 monolayer thickness, with 92% of the 1T phase. This intercalation approach not only provided a higher metallic phase portion, but also the stability of the intercalated 1T phase was greater than 300 days; however, the flake size was below 1 μm. This MoS_2 nanosheet exhibited enhanced electrocatalytic activity for the HER in both acidic and alkaline electrolytic media and, importantly, the observed performance was much higher than the 1T-MoS_2 nanosheets synthesized using the *n*-butyl lithium intercalation technique.[149]

While observing these high yielding top-down intercalation strategies, two limitations are commonly encountered: the lateral size of the obtained flake is still in the nanometre-size region and the complete phase purity of the 1T phase (complete 100% transformation from 2H→1T phase) is not ensured in any of the resultant TMD nanosheets. Recently, Patlolla Sai Kiran *et al.*[150] reported a direct single-step plasma-spray exfoliation technique for the fabrication of mono- to trilayered, ultrathin (1–2.6 nm) MoS_2 nanosheets with 100% phase purity of the 1T phase and with a lateral size of 0.6–1.6 μm (see Figure 1.14), produced without any intercalation.[150]

The synchronized exfoliation and phase transformation of MoS_2 in this technique can be attributed to two parallel processes during the fabrication of the nanosheets: (1) thermal shock in the plasma-spray process accompanied by two stages of shearing, one in the laminar region and the other in the turbulent region (see the middle row in Figure 1.14); and (2) upon exfoliation, phase transformation occurs due to the S atomic plane gliding

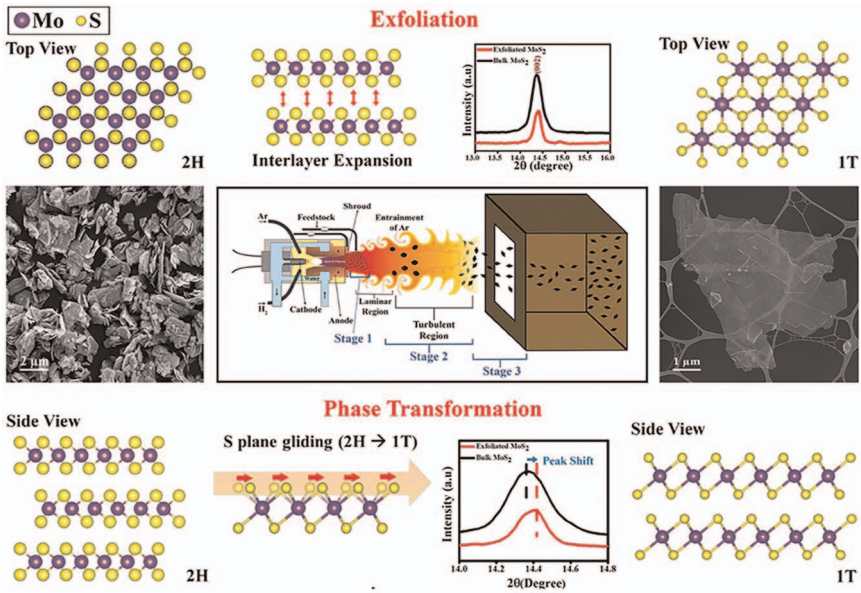

Figure 1.14 The diagrammatic representation of ultrathin 1T-MoS_2 nanosheets obtained through the direct plasma-spray exfoliation technique.[150] Reproduced from ref. 150 with permission from John Wiley & Sons, Copyright © 2024 Wiley-VCH GmbH.

induced by the high-temperature exposure of the materials and an atypical quenching rate of about 106 °C s^{-1}. The resultant ultrathin 1T-MoS_2 flakes displayed enhanced electrochemical behaviour, with a specific capacitance of about 420 F g^{-1} at a lower scan rate of 5 mV s^{-1}, which manifests as an exceptional electrode for supercapacitor applications.[150]

Nevertheless, the lateral size of the exfoliated TMDs is still in the micrometre-size region, which limits its implementation in electronic, optoelectronic, and sustainable green hydrogen generation applications. Hence, the development of advanced synthetic techniques that deliver large-scale layered TMDs with greater lateral size has become a pressing need. Ultrathin mono- or few-layered TMDs can be obtained in several bottom-up approaches, such as ALD, CVD, and radiofrequency (RF) sputtering processes.[151–153] Notably, Nikolas Aspiotis *et al.* reported uniform growth of monolayers of MoS_2 on 6-inch Si/SiO_2 wafers through ALD coupled with an annealing-based conversion technique.[154]

1.6 MXenes

1.6.1 Introduction to MXenes

MXenes represent a prominent category of 2D materials, primarily composed of carbides, nitrides, oxycarbides, and carbonitrides derived from early transition metals. Characterized by an accordion-like structure, the

typical formula of MXenes is denoted as $M_{n+1}X_nT_x$, where 'M' designates a transition metal, such as Sc, Ti, V, and Nb; 'X' indicates carbon and/or nitrogen; $n = 1$, 2, or 3; and 'T_x' signifies a functional group, such as –OH, –O, –F, –Cl, –Br, –Se, –S, and –Te, which are surface terminations in MXenes.[155]

MXenes possess a hexagonal lattice symmetry inherited from their parent MAX phase, coupled with exceptional electrical conductivity (6000–8000 S cm^{-1}) owing to their metallic backbone.[156] Abundant surface functional groups provide numerous active sites, enabling efficient surface modification. Chemical versatility arises from intrinsic composition and surface terminations, offering the potential for tailored properties. Recognized for their diverse properties, including thermal conductivity, tuneable bandgap, and mechanical strength, MXenes hold promise for applications spanning energy conversion and storage, environmental protection, transparent conductors, sensing devices, and structural composites.

1.6.2 Structure of MXenes

Given that the 'n' values for the existing $M_{n+1}AX_n$ phases can range from 1 to 3, the resulting individual MXene sheet comprises of 3, 5, and 7 atomic layers for M_2X, M_3X_2, and M_4X_3, respectively. In each scenario, the thickness of the individual MXene layers is below 1 nm, while their lateral dimensions can extend to tens of micrometres.[157] It can be said that MXenes exhibit a diverse array of structures, characterized by 2–5 layers of early transition metal atoms (M elements) linked by 1–4 layers of non-metal atoms (X = C, N, O). Additionally, combining multiple M metals within a single structure, having both in-plane and out-of-plane ordered MXenes or random solid solutions, including high-entropy MXenes containing 3–5 metals, gives rise to an infinite number of MXene structures.[158] All these various types of MXenes are summarized in Figure 1.15.

MXenes exhibit diverse structural configurations and nomenclature depending on the distribution and ordering of the transition metals within their lattice. When two different transition metals occupy M sites, forming a solid solution, the formula is represented as $(M', M'')_{n+1}X_nT_x$, with M' and M'' denoting different metals, such as $(Ti, Nb)_2C$. The concentration of each metal is expressed in decimal numbers, exemplified by $(Ti_{0.5}, Nb_{0.5})_2C$. In cases where metals exhibit in-plane ordering, forming alternating chains within the same M layer, the resulting structure is termed i-MXene, with a formula of the form $(M'_{4/3}M''_{2/3})XT_x$, where metal concentrations are fractional. i-MXenes often undergo selective etching of M'' atoms, creating ordered vacancies and leading to a simplified formula of $M'_{4/3}XT_x$.[159] Additionally, MXenes may display out-of-plane ordering, termed o-MXenes, where M'' atoms constitute inner layers, and M' atoms occupy outer layers, described by formulae of the form $(M'_2M'')X_2T_x$ and $(M'_2M''_2)X_3T_x$.[159] Understanding the terminology and structural variations of MXenes is crucial for tailoring their properties for a wide range of applications, including electronics, catalysis, and energy storage. The MXene system encompasses over a

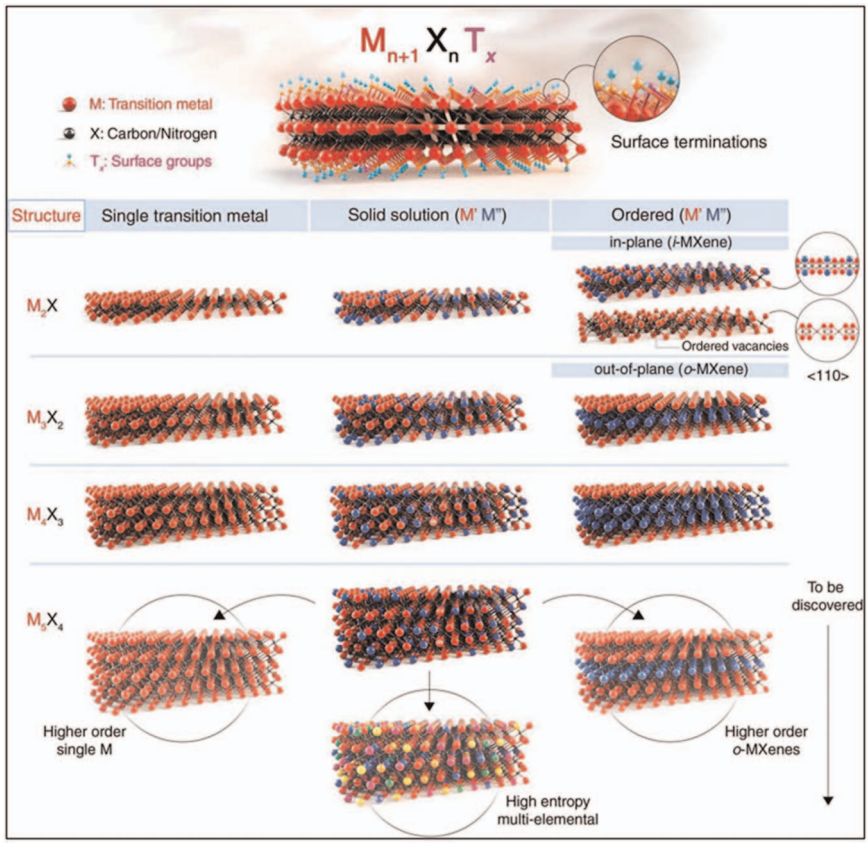

Figure 1.15 Schematic illustration of MXene structure.[202] Reproduced from ref. 202, https://doi.org/10.1007/s42247-023-00591-z, under the terms of the CC BY 4.0 license, https://creativecommons.org/licenses/by/4.0/.

thousand stoichiometric compositions, leveraging various transition metals, carbon, and nitrogen, alongside typical structures and surface terminations. With solid solutions and diverse terminations, countless 2D materials can be synthesized. Currently, over 50 MXenes are reported, and this is expected to double with advancements in computational materials science, facilitating tailored synthesis for specific applications.[160]

1.6.3 Properties of MXenes

1.6.3.1 Electronic Properties

MXenes have a broad spectrum of electronic characteristics, ranging from topological insulation to semiconductivity and metallic behaviour. This broad spectrum of features is provided by their flexible control over thickness, myriad surface functionalization possibilities, and a broad span of

compositional ranges. Electrical conductivity depends on the defects present in the MXene structure.[161] According to Zhang *et al.*[162] MXenes terminated with electronegative groups, such as –OH, have practically free electron states that are parallel to the surface and located outside the surface atoms. These states provide extremely effective electron transport through transmission channels induced by clustering in areas of maximal positive charge. Furthermore, their experiments revealed that O-terminated MXenes exhibit lower electrical conductivity compared to those terminated with F and OH.[162] Investigations employing coherent transport computations utilizing the non-equilibrium Green's function (NEGF) approach have revealed that metallic MXenes demonstrate substantial conductivity, positioning them as promising candidates for electronic components, such as transistors, capacitors, supercapacitors, electrical sensors, *etc.*[163]

While most MXenes retain their metallic properties, M'_2CO_2 ($M' = Ti, Zr, Hf$) and Sc_2CX_2 ($X = O, F, OH$) are found to be semiconductors, with energy bandgaps of 0.24, 0.88, 1.0 eV and 1.8, 1.03, 0.45 eV, respectively, estimated using the general gradient approximation (GGA).[164] $Sc_2C(OH)_2$ has a direct bandgap while the others have an indirect bandgap.

Khazaei *et al.*[164] investigated the effect of functionalization on electronic structures of pristine MXenes to assess the semiconducting nature of the materials. In pristine Ti_2C MXene, the d bands of transition metals dominate, situated above the p bands of carbon and nitrogen, and showcasing metallic behaviour. Upon functionalization, transition metals donate electrons, shifting the Fermi energy to the gap's centre, between the d orbitals and p bands, and promoting semiconducting properties. Figure 1.16a–c shows the density of states of pristine Ti_2C, illustrating its metallic nature, with Ti d and C p orbitals being prominent. After F adsorption, Ti_2C remains metallic (see Figure 1.16d), with additional bands of F p orbitals added to existing Ti d orbitals. Conversely, O adsorption induces a downward Fermi energy shift towards the centre of the bandgap, leading to semiconducting behaviour, as seen in Figure 1.16e. This electronic restructuring underscores the pivotal role of functionalization in modulating the electronic properties of the MXene, influencing its utility in diverse applications.

Chen *et al.*[165] devised a tight binding model using $d_{z^{2-}}$, $d_{xy^{-}}$, $d_{x^2-y^{2-}}$ orbitals on a triangular lattice to assess $Mo_2MC_2O_2$ ($M = Ti, Zr,$ or Hf) properties. These MXenes, featuring dual transition metal elements in an ordered configuration, exhibit robust quantum spin Hall (QSH) insulator behaviour. Notably, the atomic SOC strength of M significantly influences the topological gap (in the range of 0.1–0.2 eV) at the Γ point, which is large enough to display QSH effects at room temperature, as depicted in Figure 1.17. Additionally, such double transition metal MXenes possess oxygen-covered surfaces, rendering them antioxidative and stable when exposed to air.[165] Reports have also shown that MXenes such as $Sc_2C(OH)_2$ can be transformed from a trivial insulator to a topological insulator by inducing an electrical field amplitude, proving the versatility of this 2D material.[166]

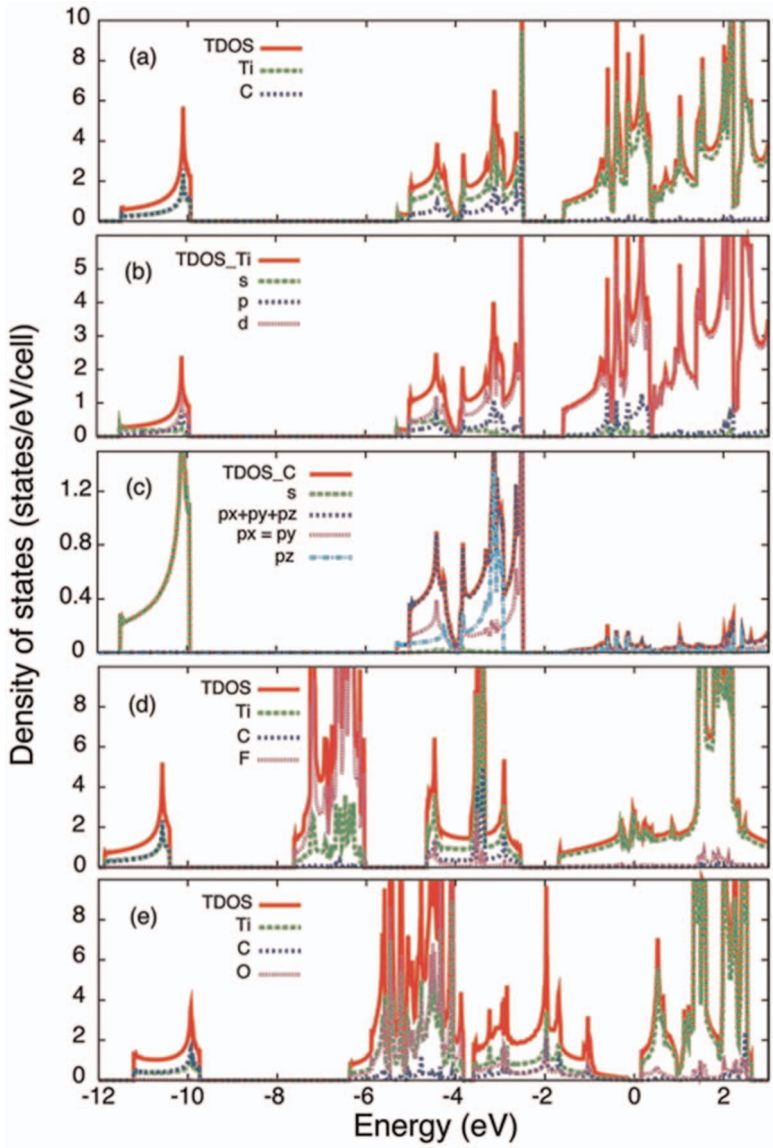

Figure 1.16 (a) DOS of Ti_2C and (b) and (c) the DOS on atomic orbitals of Ti and C atoms, respectively. (d) and (e) DOS of Ti_2CF_2 and Ti_2CO_2, respectively. Fermi energy is at zero. For the semiconductors, it is shifted to the centre of the gap.[164] Reproduced from ref. 164 with permission from John Wiley & Sons, Copyright © 2013 WILEY-VCH Verlag GmbH & Co. KGaA, Weinheim.

MXenes with partially occupied nearly free electron states, offer low-resistance pathways, especially under low bias voltages, making them viable for low-power nanoelectronic devices requiring efficient electron transport.[163] First principles

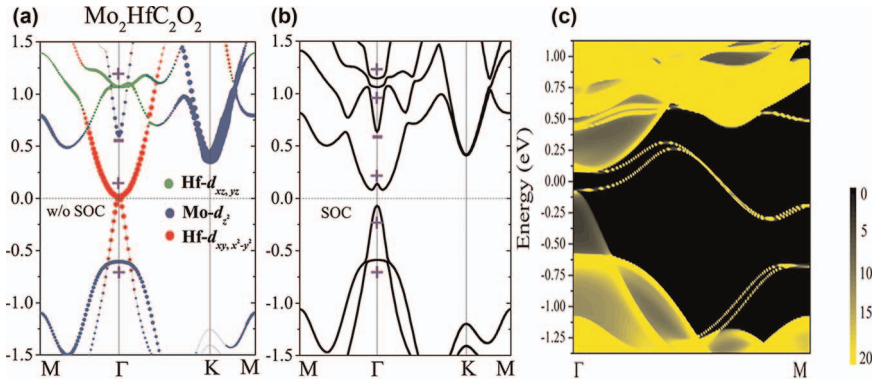

Figure 1.17 Electronic band structure of $Mo_2HfC_2O_2$ computed (a) without SOC and (b) including SOC. (c) Edge states connecting the bulk valence and conduction bands and only touching at the M point.[165] Adapted from ref. 165 with permission from American Chemical Society, Copyright 2016.

calculations have elucidated that electron conduction in layered $Ti_3C_2T_2$ (T = F, OH, or O) MXenes is markedly anisotropic due to disparities in the effective masses of electrons and holes along distinct lattice orientations. This directional behaviour has been experimentally validated through *in situ I–V* measurements, demonstrating that lateral electrical conduction surpasses vertical conduction by at least an order of magnitude.[167] Additionally, investigations have explored the impact of gas molecule adsorption on electron transport in MXenes. For instance, Ti_2CO_2 has been investigated as a prospective gas sensor, with NH_3 chemisorption with an apparent charge transfer of 0.174*e*. This responsiveness to gas adsorption underscores the potential of MXenes as highly discerning and sensitive gas sensors for various gases, such as O_2, N_2, NO_2, CO_2, CO, CH_4, and H_2.[168]

1.6.3.2 *Magnetic Properties*

According to spin-polarized density functional computations, many pristine and functionalized MXenes exhibit non-magnetic ground states due to the strong covalent bonding between the transition metal and the X element, as well as the attached chemical groups. However, the covalency of these bonds can be tuned, leading to the release of d electrons and, as a result, producing magnetism, even in non-magnetic systems.[169] Specific functionalized MXenes, including Ti_2NO_2, Cr_2NO_2, and all Mn_2CT_2 and Mn_2NT_2 systems, have been proposed to demonstrate magnetic moments of up to 3 μ_B (potentially displaying such properties at room temperature), making them ideal for spintronic devices. Furthermore, substantial magnetic moments can be induced in 2D MXenes through the application of tensile/compressive strain or the introduction of Cr/Mn elements *via* doping.[170]

Certain MXenes, such as M_2X (M = Cr, Mn, Ti and X = C, N), exhibit intrinsic magnetism due to transition metal defects in monolayers or surface

terminations. While Cr_2N and Mn_2C are antiferromagnetic, others show ferromagnetic behaviour, as dictated by the electronic states and interactions among the transition metal ions and ligands. According to the Goodenough–Kanamori rule, antiferromagnetic tendencies arise from ligand-mediated superexchange interactions,[171] while ferromagnetism can stem from direct exchange interactions or double-exchange interactions promoting favourable spin alignments. Conversely, localized electron behaviour may weaken double-exchange interactions, leading to antiferromagnetic behaviour driven by superexchange interactions.[172,173]

Recently, magnetic MXenes with half-metallicity have garnered attention for their unique property of spin-polarized electrons at the Fermi level, where one spin channel behaves as a metal and the other as a semiconductor. While surface functionalization can alter their magnetic and electronic characteristics, MXenes with Cr and Mn retain their magnetism even after surface passivation, unlike others. Functional groups (–F, –H, –OH, or –Cl) can influence their magnetic couplings and electronic structures, transforming MXenes such as Cr_2C from ferromagnetic half-metals to antiferromagnetic semiconductors, or Cr_2N from antiferromagnetic metals to ferromagnetic half-metals upon surface passivation (with –O).[174]

1.6.3.3 Optical Properties

The enhanced optical characteristics of MXenes, particularly $Ti_3C_2T_x$, are attributed to the layered structure and favourable electron transport properties occurring due to the high density of states at the Fermi level. Theoretically, the imaginary component of the dielectric function tensor, reveals insights into the optical properties, such as transmittance, absorption, and reflection, across various photon wavelengths.[175] $Ti_3C_2T_x$ films exhibit light absorption within the UV–visible region spanning 300 to 500 nm, while maintaining high transmittance levels of up to 91.2% for films with a thickness of 5 nm. Moreover, they have a notable, broad absorption band typically occurring around 700–800 nm. Importantly, the optimization of transmittance values is feasible by adjusting both the film thickness and ion intercalation processes.[161,176] It was found that DMSO/hydrazine/urea-treated $Ti_3C_2T_x$ has decreased transmittance, while, on the other hand, tetramethyl ammonium hydroxide-intercalated $Ti_3C_2T_x$ shows increased transmittance from 74.9 to 92%.[177]

The analysis by Berdiyoroy *et al.*[178] revealed that at lower photon energies (E), the terminations induced a decrease in the refractive index (n), while at higher E values (0.1 eV), n exhibited augmentation. Furthermore, surface terminations led to a general reduction in extinction coefficient (k) across most of the photon energy spectrum, as shown in Figure 1.18.

Notably, at significantly higher photon energies ($E < 0.5$ eV) the terminations precipitated heightened absorption compared to the pristine MXene. Moreover, within the ultraviolet segment of the spectrum (5 eV $< E <$ 10 eV), all surface terminations showed greater reflectivity relative to the pristine

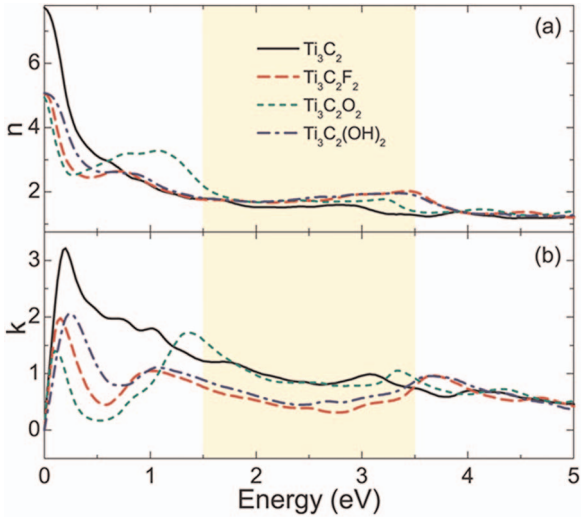

Figure 1.18 (a) The refractive index, *n*, and (b) the extinction coefficient, *k*, as a function of photon energy for $Ti_3C_2T_2$ MXene.[178] Adapted from ref. 178, https://doi.org/10.1063/1.4948799, under the terms of the CC BY 4.0 license, https://creativecommons.org/licenses/by/4.0/.

MXene.[178] MXenes exhibit photoluminescence (PL) from the formation of a direct energy bandgap due to the reduction in system size, enabling radiative electronic transitions. Additionally, MXene nanosheets can induce fluorescence quenching effects, which are utilized in fluorescence resonance energy transfer (FRET) for molecular imaging.[179]

1.6.3.4 Plasmonic Properties

Mauchamp *et al.*[180] utilized high-resolution transmission electron energy-loss spectroscopy (EELS) to demonstrate that the surface plasmon frequency of Ti_3C_2 MXene sheets can be adjusted in the mid-infrared range by manipulating sheet functionalization and thickness.[180] Interestingly, the bulk plasmonic behaviour remains consistent regardless of the number of layers, making MXenes versatile for photon detection applications, as they need not strictly be in a single layer.[181] The presence of bulk plasmon excitations appears to be unaffected by the number of MXene sheets stacked together, possibly due to weak coupling between the $Ti_3C_2T_x$ sheets.

Notably, various experiments have highlighted the exceptional plasmonic properties of MXenes. In particular, $Ti_3C_2T_x$ nanosheets show significant enhancement factors for surface-enhanced Raman spectroscopy (SERS) when combined with noble metals, such as Ag, Au, and Pd.[182] Moreover, MXene substrates without noble metals have been fabricated for enhanced Raman signal detection, which is attributed to interband transitions and subsequent charge transfer mechanisms. In the context of photodetectors,

MXenes offer advantages over highly conductive materials, which often produce high dark currents. Recent studies have demonstrated the potential of less-conductive MXene (Mo_2CT_x) as a promising plasmonic photodetector in the visible light range, achieving high responsivity and detectivity. Surface plasmon modes in Mo_2CT_x facilitate efficient hot-electron generation, contributing to its detection mechanism.[183]

Compared to gold nanomaterials, MXene flakes provide larger surface areas for molecule adsorption and strong electrostatic interactions due to their negatively charged surface. The dominant mechanism for MXene SERS is the chemical mechanism, driven by charge transfer from the MXene to dye molecules.[184] MXenes have demonstrated significant enhancements in detecting various molecules, including organic contaminants, highlighting their potential in biomedical imaging, environmental analysis, and food safety monitoring applications.[185]

1.6.3.5 Mechanical Properties

MXenes are characterized by robust M–N and M–C bonding, making them mechanically stable materials. This strong bonding is essential for their structural integrity and determines their mechanical behaviour.[186] The atomic layer count (n) in MXene ($M_{n+1}X_n$) refers to the number of atomic layers stacked together in the material's structure. Generally, an increase in n leads to a decrease in Young's modulus, *i.e.* toughness and durability.[186,187]

Simulation studies show MXenes possess twice the elastic parameters of MAX systems and other 2D materials, such as CdS_2, indicating high stiffness, which is ideal for structural applications. Despite slightly lower elastic properties than graphene, MXenes exhibit exceptional bending characteristics, surpassing graphene, and making them suitable for flexible applications, such as composites.[188,189] Superior interaction with polymeric matrices enhances mechanical properties, as demonstrated by $Ti_3C_2T_x$–PVA composites, which show a 4.1 times higher tensile strength than $Ti_3C_2T_x$ due to strong interfacial interaction.[190]

Titanium-based MXene disks exhibit hydrophilic behaviour, with contact angles typically ranging from 25 to 40 degrees,[191] making MXenes suitable for applications where interaction with water or aqueous environments is necessary, such as in biomedical devices or water purification systems. Nitride-based MXenes tend to have higher Young's modulus values compared to carbide MXenes,[192] while the latter are known to be mechanically more stable.[193] Interestingly, a relatively uncommon negative Poisson ratio was anticipated for W_2C, suggesting potential uses in advanced technical sectors, such as in components resistant to fractures in automobiles and aircraft.[194] MXenes terminated with –O groups tend to exhibit greater toughness and decreased critical deformations compared to those terminated with –F and –OH groups. This suggests that surface functionalization can be used to tailor MXene properties for specific applications, especially flexible electronics.[195]

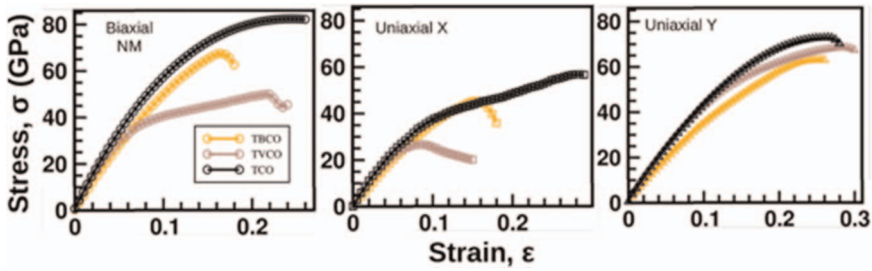

Figure 1.19 The stress–strain curve of Ti_2CO_2, and $Ti_2(C_{0.5},B_{0.5})O_2$ under biaxial and uniaxial tensile strains along the x and y directions, respectively.[196] Reproduced from ref. 196 with permission from American Physical Society, Copyright 2017.

Boron doping of MXenes replaces carbon atoms, enhancing both the mechanical and electronic properties compared to pristine MXenes. This increased strain tolerance is attributed to the weaker bonding between titanium (Ti) and boron (B) compared to that between Ti and carbon (C). For instance, boron-doped Ti_2CO_2 MXene exhibits increased strain tolerance, making it more resistant to deformation. The introduction of boron alters the electronic band structure, potentially enhancing electrical performance.[196]

Theoretical calculations have further supported the notion that Ti_2CO_2-based composites can withstand significant strain under both uniaxial and biaxial tension,[197] as shown in Figure 1.19, indicating their potential for use in high-stress environments, and thus can find applications in aerospace, automotive, and electronics industries.

1.6.4 Synthesis of MXenes

Synthesis of MXenes can be grouped into two, diverse, top-down and bottom-up methods.

1.6.4.1 Top-down Methods

1.6.4.1.1 Etching. MXenes are derived from MAX phases by selectively removing the 'A' layers, which are typically group IIIA or IVA elements. MAX phases consist of 2D layers of early transition metal carbides and/or nitrides held together by an 'A' element. The bonding in MAX phases exhibits a combination of covalent, metallic, and ionic characteristics, with predominantly metallic M–A bonds. The etching process from MAX to MXene requires careful control of temperature and etchant reactivity, to preserve the 2D structure of the $M_{n+1}X_n$ layers.[158] During etching, the newly exposed M element surface undergoes immediate functionalization facilitated by surface-terminating species from the etchant, which differ from those in the original MAX phase. These surface terminations,

emphasized by the MXene formula $M_{n+1}X_nT_x$, play a crucial role in defining MXene properties.

The first reported synthesis of MXene in 2011 involved etching Ti_3AlC_2 MAX phases using 50% HF acid to selectively remove aluminium (Al), forming Ti_3C_2. Due to the hazardous nature of HF, safer techniques have been developed, such as *in situ* HF preparation preceding the etching process or using alternative acid/fluoride salt combinations. Various fluoride salts can substitute for HF in etchant solutions, enabling the synthesis of diverse multilayered MXenes under controlled etching conditions. MXenes produced *via* the HCl/LiF method readily delaminate into single-layer nanosheets with unique shapes, while *in situ* HF etching enriches MXenes with surface functionalities such as –F, –OH, and –O. However, drying times are extended due to interlayer water molecule intercalation, and yield constraints may arise from unetched MAX phase residues.[198]

1.6.4.1.2 Electrochemical Etching. The electrochemical etching method selectively removes the aluminium atomic layer from MAX phases under specific voltage conditions, yielding MXenes (see Figure 1.20). Researchers have explored various electrolytes (NaCl, HCl, and HF) and electrode configurations to enhance the etching process and minimize the formation of undesired carbide-derived carbons (CDCs). Notably, a three-electrode system employing 0.6 V etched the MAX phase, utilizing bulk Ti_2AlC as the working electrode. The system consisted of Ag/AgCl as the reference electrode and Pt as the counter electrode, with HCl as the electrolyte. This

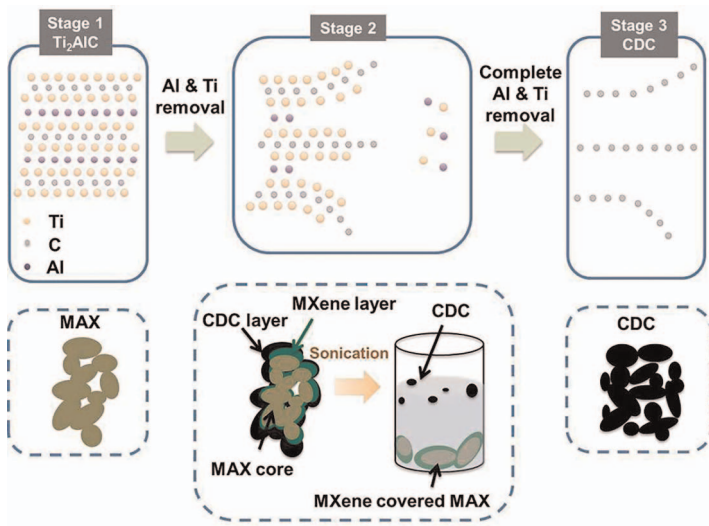

Figure 1.20 Electrochemical etching technique for obtaining MXenes.[295] Reproduced from ref. 295 with permission from the Royal Society of Chemistry.

resulted in Ti_2CT_x MXene formation, with the CDC hindering further etching. However, challenges include the concurrent formation of CDC layers alongside MXenes and relatively low yield. To facilitate the production of MXenes on a large scale, endeavours to tackle these challenges involve optimizing the compositions of electrolytes and investigating intercalation techniques.[199]

1.6.4.1.3 Mechanical Exfoliation. Mechanical exfoliation involves mechanically separating (peeling or rubbing) material layers from a bulk substrate. This technique extracts 2D flakes from 3D MAX phase crystals. Theoretically, the varying strengths of bonding permit breaking metal (M) and A (usually aluminium or silicon) layer bonds under tensile stress.[200] Recently, Gkountaras *et al.* experimentally validated this theoretical understanding. They employed the adhesive tape method to mechanically exfoliate four MAX phase single crystals, producing MXene flakes as thin as half a unit cell. Remarkably, even chemically non-etchable MAX phase crystals, such as Cr_2AlC, Ti_2SnC, and $Mo_4Ce_4Al_7C_3$, were successfully exfoliated.[201]

1.6.4.1.4 Intercalation. Intercalation plays a crucial role in the synthesis and processing of MXenes, facilitating the separation of MXene layers and widening the interlayer spacing. By introducing intercalation materials between the layers of MXenes, the bonds between the layers are weakened, allowing for easier delamination, by increasing the interlayer spacing, into individual 2D sheets. This process is essential for obtaining functional and processable MXene sheets that are electrically stabilized and free from clumping or aggregation.[202]

Dimethyl sulfoxide (DMSO), for instance, was one of the initial intercalants used to expand spacing between layers in $Ti_3C_2T_x$ MXene synthesized with fluorine-based salts.[203] Tetraalkylammonium hydroxides (TBAOH and TMAOH) are another group of compounds utilized to exfoliate layered oxides, leading to delamination and expansion through ion exchange.[204] Cations such as Na^+, Li^+, K^+, Mg^{2+}, NH^{4+}, and Al^{3+} can be intercalated into MXene layers, widening the interlayer spacing. Additionally, polar organic molecules of different sizes can also be intercalated, further increasing the interlayer spacing.[205] For example, when $Ti_3C_2T_x$ is intercalated with hydrazine, its lattice parameter increases from 19.5 Å to 25 Å.[206] Techniques such as ultrasonication are utilized to blend the intercalant into MXene sheets, determining the size and concentration of the resulting flakes.[202]

1.6.4.2 Bottom-up Synthesis

1.6.4.2.1 Urea Glass Method. The urea glass method synthesizes MXene materials from metal precursors such as metal chlorides (*e.g.* $MoCl_5$). The process involves mixing the precursor with ethanol to form metal orthoesters, and then adding solid urea as a nitrogen source. After complete dissolution, the mixture undergoes calcination around 800 °C in an

inert atmosphere to form MXene layers, yielding silvery black granules (*e.g.* Mo_2C/Mo_2N).[207]

1.6.4.2.2 Chemical Vapor Deposition. The CVD process, depicted in Figure 1.21, involves depositing thin films from vapor onto a substrate surface. For instance, Xu *et al.*[208] used Cu and Mo foils with methane gas as the carbon source. The substrate is heated to temperatures exceeding the melting point of the metal components (1085 °C), allowing metal atoms to diffuse and react with carbon atoms, and forming MXenes, such as orthorhombic α-Mo_2C.[208] The thickness and lateral size of the MXene crystals can be adjusted by varying the concentration of methane or other precursor gases used during the CVD process. Additionally, heterostructures like Mo_2C/graphene have been fabricated using CVD, and show enhanced performance compared to pure Mo_2C electrodes.[209,210] Transition metals, such as tungsten and tantalum, have also been employed to synthesize ultrathin crystals of tungsten carbide (WC) and tantalum carbide (TaC) *via* CVD.[208] Although CVD-grown materials offer advantages, such as large size and fewer defects, the high fabrication costs limit their widespread commercialization.

1.6.4.2.3 Plasma-enhanced Pulsed Laser Deposition. Pulsed laser deposition (PLD) offers a bottom-up approach for synthesizing ultrathin 2D layered films, such as complex oxides, and presents advantages over conventional methods, such as CVD. Plasma-enhanced PLD (PEPLD) enhances film formation by incorporating a plasma source that interacts with laser-ablated material, facilitating new film formation or modified layer deposition. Energetic ions in the plasma improve deposition rates and film quality.

Zhang *et al.*[211] reported the PEPLD process for fabricating large-area, high-quality 2D, face-centred cubic (FCC)-structured Mo_2C crystals on a sapphire (0001) substrate. They found that ionized CH_4 plasma plays a crucial role in depositing 2D FCC-structured Mo_2C crystals, as no Mo_2C was deposited

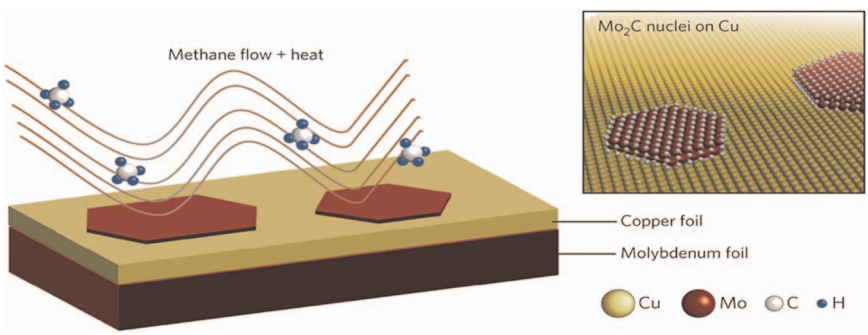

Figure 1.21 CVD process for the synthesis of MXenes.[296] Reproduced from ref. 296 with permission from Springer Nature, Copyright 2015.

without ionized CH_4 plasma. The thickness of the Mo_2C film could be tuned from 2 to 25 nm by adjusting parameters. The crystal quality degraded with decreased deposition temperature, but films grown at 700 °C exhibited high-quality single crystals.[212]

1.6.4.2.4 Spray Coating. In 2016, a new method was introduced utilizing spray coating of a colloidal delaminated $Ti_3C_2T_x$ suspension to create transparent, conductive films with a consistent concentration of 3.0 mg mL^{-1} on large substrates at room temperature.[177] Additionally, flexible substrates, such as polyester layers, showed promise for producing transparent $Ti_3C_2T_x$ thin films *via* spray coating, retaining their integrity even after minor bending. These $Ti_3C_2T_x$ films displayed superior optoelectronic properties compared to solution-processed transparent graphene films, suggesting their potential for applications in transparent conductors for electronic devices, sensors, and electrochromic applications.[202]

1.6.5 Applications of MXenes

1.6.5.1 Adsorption of Pollutants

The narrow interlayer gap (<2 Å) makes MXene nanosheets well suited for capturing heavy metal ions present in industrial effluent, and is further enhanced by surface-functionalized characteristics.[213] Titanium-based MXenes, particularly $Ti_3C_2T_x$ nanosheets, have shown efficacy in removing both reduced Cr(III) ions and Cr(VI) ions through reduction-adsorption mechanisms.[214] Functionalized MXene nanocomposites have effectively removed various heavy metal ions through adsorption, offering potential solutions for water purification challenges. $Ti_3C_2T_x$ MXene-based films also exhibit capabilities in eliminating Au(III), Pd(II), Ag(I), and Cr(VI) ions, with the potential for reuse after cleaning with HCl and NaOH solutions.[215]

MXenes have emerged as highly effective adsorbents for detoxifying nuclear waste, particularly in adsorbing Cs(I), Th(IV), and U(VI).[216] Experimental results and theoretical predictions using DFT calculations have demonstrated the efficient removal of U(VI) ions by $V_2C(OH)_2$ nanosheets.[217] Wang *et al.*[218] developed DMSO-intercalated $Ti_3C_2T_x$ nanosheets, significantly increasing the uranium ion adsorption capacity due to hydration and intercalation stimulation.

Recent studies by Meng *et al.*[219] and Wu *et al.*[220] have demonstrated the potential of MXene-based materials in effectively removing organic pollutants. The potential of $Ti_2C_3T_x$ MXene in effectively removing organic components, such as phenol and other pharmaceutical components, in specific pH conditions was demonstrated by Wu *et al.*[220] and Kim *et al.*,[221] respectively. Additionally, $Ti_3C_2T_x$MXene showed significant promise in adsorbing dyes.[222,223]

1.6.5.2 Photocatalytic Hydrogen Evolution Reaction

TiO_2 is a widely studied semiconductor for photocatalytic hydrogen evolution, and is valued for its abundance and effectiveness. However, its pure form has limitations such as low light utilization and rapid carrier recombination.[224] To address this, Li *et al.* developed Ti_3C_2–TiO_2 nanoflowers, enhancing the reaction with optimal hydrogen and oxygen production rates.[225] MXenes, including Nb_2CT_x, have been combined with metal oxides, like Nb_2O_5, to improve photocatalytic efficiency.[226] Metal doping strategies, such as $Cu/TiO_2@Ti_3C_2T_x$, have also been utilized to enhance TiO_2 catalytic activity by enabling the photoinduced reduction of Cu_2O to Cu.[227] In the $Ti_3C_2@TiO_2@MoS_2$ system, 2D Ti_3C_2 MXene and MoS_2 nanosheets served as electron mediators, forming heterojunctions that enhanced the photocatalytic activity by facilitating effective electron migration and increasing the surface area and water adsorption capability.[228]

Metal sulfides, such as CdS, ZnS, and In_2S_3, play a vital role in photocatalysis due to their band positions and visible light responsiveness. However, challenges, such as carrier recombination and photocorrosion, limit their efficacy. To overcome these obstacles for enhancing hydrogen generation, researchers have created multidimensional heterojunction photocatalysts by integrating CdS nanorods with Ti_3C_2 MXene nanosheets.[229] Theoretical calculations show that O-terminated Ti_3C_2 demonstrates superior photocatalytic activity, attributable to its high Fermi levels (1.8 eV).[230] Ternary composites, such as $Zn_2In_2S_5/Ti_3C_2(O, OH)_x$ and $CdLa_2S_4/Ti_3C_2$, exhibit enhanced photocatalytic properties due to strong interfacial interactions.[231,232] Additionally, exfoliated 2D Mo_2C MXene acts as a cocatalyst, enhancing H_2 production rates through rapid charge transfer and active site provision.[233]

Figure 1.22 depicts the mechanistic path for hydrogen generation on $Ti_2C/g\text{-}C_3N_4$ photocatalyst. The coupling of the 2D $g\text{-}C_3N_4$ semiconductor

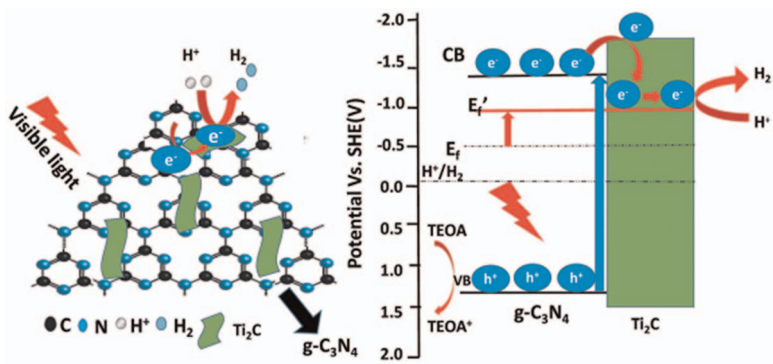

Figure 1.22 Mechanistic strategy for photocatalytic H_2 evolution using Ti_2C cocatalyst and $g\text{-}C_3N_4$ nanosheets.[234] Reproduced from ref. 234 with permission from the Royal Society of Chemistry.

and metallic Ti_2C as a cocatalyst enhances charge separation and electron transport to the metallic Ti_2C material, resulting in substantial charge buildup and a negative shift of the Ti_2C Fermi level. Furthermore, the Fermi level of Ti_2C/g-C_3N_4 composites is closer to the conduction band of g-C_3N_4, implying that electrons accumulate on the Ti_2C/g-C_3N_4 interface, which is directly connected to the improved photocatalytic hydrogen evolution.[234] A Schottky junction combining 2D Ti_3C_2 MXene with O-doped g-C_3N_4 was also utilized in the photocatalytic-based HER. This composite exhibited nearly a doubled hydrogen evolution rate (25 124 $\mu mol\, g^{-1}\, h^{-1}$) compared to pristine O-doped g-C_3N_4 (13 745 $\mu mol\, g^{-1}\, h^{-1}$) and Ti_3C_2 MXene/pristine g-C_3N_4 (15 573 $\mu mol\, g^{-1}\, h^{-1}$). The enhanced performance was attributed to the synergistic effect of the intimate 2D/2D interfacial contact and the formation of the Schottky junction, which facilitated shorter charge transport distances and efficient separation of photogenerated charges.[235]

1.6.5.3 Photocatalytic CO_2 Reduction

Photocatalytic CO_2 reduction has emerged as a crucial area of research to combat the greenhouse effect and energy shortages. Recent investigations propose MXenes as potential cocatalysts for photocatalytic CO_2 reduction due to their remarkable physicochemical properties.[236] Among MXenes, $Ti_3C_2T_x$ stands out for its superior performance as a cocatalyst in CO_2 reduction, surpassing graphene and noble metals. $Ti_3C_2T_x$ facilitates fast separation of photogenerated charge carriers, leading to high photoconversion efficiencies. Additionally, $Ti_3C_2T_x$ offers a large surface area, active adsorption sites, and good interface contact for efficient charge carrier separation. The presence of various terminal functional groups further enhances its catalytic activity.

Studies have shown that the surface-alkalized Ti_3C_2–OH/ZnO composite exhibits enhanced CO_2 reduction rates, with promising results achieved in generating organic products, such as CO (30.30 $\mu mol\, g^{-1}\, h^{-1}$) and CH_4 (20.33 $\mu mol\, g^{-1}\, h^{-1}$).[237] Li *et al.*[238] synthesized g-C_3N_4/MXene (MCT) for efficient photocatalytic CO_2 reduction. The mesoporous structure of g-C_3N_4 facilitated gas molecule adsorption due to its large surface area, while enhanced contact between $Ti_3C_2T_x$ and mesoporous g-C_3N_4 led to improved charge separation, resulting in the generation of various organic products, with CO and CH_4 as the dominant products. Mesoporous MCT exhibited 2.4 times more CH_4 production than mesoporous g-C_3N_4 (MC), indicating its excellent selectivity and activity.[238]

1.6.5.4 Energy Storage

MXenes have garnered attention as promising materials for electrodes in various types of ion batteries due to their high electrical conductivity and ion diffusion properties. Monolayers (ML) of $Ti_3C_2T_z$ have shown a capacity of approximately 150 $mA\, h\, g^{-1}$ at 260 $mA\, g^{-1}$ in lithium-ion (LIBs)[239] and

100 mA h g^{-1} at 100 mA g^{-1} in sodium-ion batteries (SIBs).[240] However, electrodes made from single-layered flakes, which have greater exposure to the electrolyte, are expected to exhibit even higher capacities. NaOH-treated MXene flakes showed capacities of about 180 mA h g^{-1} (acid-treated)[239] and 230 mA h g^{-1} (base-treated)[240] in SIBs. Ren and Xie's method involved vacuum filtering films made of porous $Ti_3C_2T_z$ flakes and carbon nanotube spacers, yielding electrodes with a capacity of 700 mA h g^{-1}, nearly four times higher than the monolayer counterparts.[241] MXenes also demonstrate excellent performance in supercapacitors, primarily utilizing pseudocapacitance from surface redox reactions. MXenes exhibit high volumetric and gravimetric capacitances, surpassing traditional materials, such as RuO_2 and activated carbon. Lukatskaya *et al.*[242] reported that Ti_3C_2 in a microporous architecture showed exceptional capacitance of 300 F g^{-1} at low scan rates, highlighting the significant potential of MXenes in energy storage applications.

1.7 Transition Metal Oxides

As mentioned in the previous sections, there are a plethora of 2D materials that have been targeted recently for energy transition, and TMOs are an interesting example of such materials. To understand why TMOs seem to be perfect tailor-made materials, it is worth digressing to provide an overview of the electrochemical OER in water and the mechanism of ion storage in batteries and supercapacitors. This digression aims at making a case for TMOs as promising candidates for energy conversion and storage applications, and describes what makes these 2D materials particularly interesting and preferred against their bulk counterparts. Hydrogen stands out as a promising energy carrier and has limitless potential to change the manufacturing, logistics, power, and chemical industries. Most current hydrogen needs are fulfilled through methane steam reforming, dry methane reforming, reverse water gas shift reaction, and green hydrogen, which accounts for a much smaller percentage.

As of 2015, hydrogen production through green routes represented only 4% of the global hydrogen needs, which is expected to grow to 22% by 2050.[243] However, there are some major issues related to scaling up the electrolysis process. One of the prime bottlenecks is the slow oxygen evolution reaction (OER); such a sluggish process is also found in rechargeable metal–air batteries. Therefore, it makes perfect sense to synthesize a catalyst that can boost the OER. Understanding the mechanism of the OER is vital to understand which materials have shown great results and how well TMOs work. There are two generally proposed mechanisms for the OER in alkaline conditions: (1) the adsorbate evolution mechanism (AEM) and (2) the lattice oxygen evolution mechanism (LOEM). In the AEM, the reaction is initiated by adsorption of OH^- ion onto the active metal site, which results in M–OH, followed by H^+ and e^- removal to form M–O; this species then reacts again with OH^- ion, forming M–OOH, which in turn reacts with another OH^- to

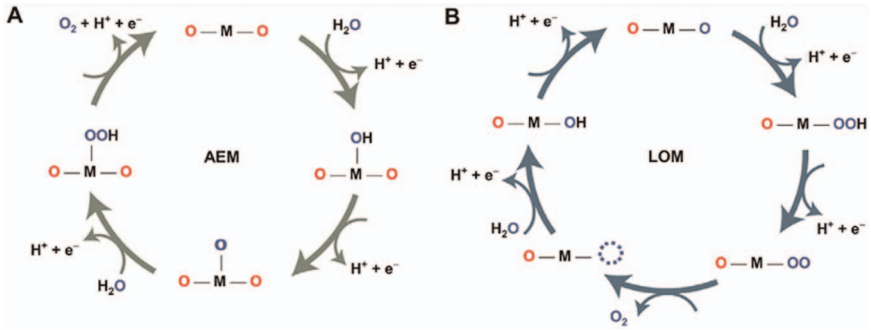

Figure 1.23 Mechanisms of the OER. (A) The mechanism of AEM and (B) the mechanism of LOM in alkaline water electrolysis.[244] Reproduced from ref. 244 with permission from John Wiley & Sons, Copyright © 2022 Battelle Memorial Institute. Advanced Functional Materials published by Wiley-VCH GmbH.

regenerate the active site and produce O_2 and H_2O. The LOEM mechanism suggests the direct involvement of oxides. In contrast to the AEM, lattice oxygen in the TMO catalyst plays a direct role in the reaction as it evolves during the reaction, resulting in oxygen vacancies, which are filled by OH^- from the electrolyte and, after subsequent deprotonation, the catalyst is regenerated[244] (see Figure 1.23 for consolidated reaction schemes). It is evident from the LOEM mechanism that oxides play a huge role in the OER. For further reading on the OER and other materials that are suitable for it, we direct our readers to these great resources in ref. 245 and 246.

For metal-ion batteries, 2D-layered TMO materials are favoured due to their large interlayer spacing, facilitating repeated ionic intercalation/deintercalation of ions between the cathode and anode. This directly results in long life cycles and also expands the possibilities of storage of intercalates with larger ionic radii. This allows us to explore battery chemistries beyond that of Li-ion technology. Additionally, TMOs offer excellent chemical and mechanical stability, facilitating longer charging/discharging cycles with minimal volume expansion, ensuring safety by preventing any possible hazardous incident.[247]

While there are many possible permutations of TMOs, such as perovskite oxides (ABO_3), spinel oxides (AB_2O_4), Ruddlesden–Popper oxides ($A_{n+1}B_nO_{3n+1}$), *etc.*, which exhibit properties different from their bulk counterparts and giving rise to intriguing characteristics, our main focus in this section will be binary oxides (A_xO_y). Although there has been monumental progress in this field, it has been observed that 2D TMOs are overlooked compared to other members of the family of 2D materials. In the following sections, we briefly explain the structure and electronic properties of 2D layered TMOs (binary oxides). Although TMOs are plagued with issues of poor electronic conductivity,[248] in subsequent sections we have attempted to discuss some interesting strategies to increase their

conductivity that are incorporated automatically into their synthesis routes, and we also discuss the outcomes of the strategies employed .

1.7.1 Crystal Structure of 2D Layered TMOs

In the 2D sheet-like structure of TMOs, the in-plane atoms consisting of transition metal (M) and oxygen (O) are connected to each other by a covalent bond (M–O–M), and such layers are held together by vdW forces. Transition metals exhibit a large number of oxidation states, on complete or partial filling of the d orbitals, and hence a change in the structure of the materials, such as in vanadium oxide, which exists in four main states: VO, V_2O_3, VO_2, and V_2O_5.[249]

Furthermore, TMOs exist in various polymorphs. For example, titanium oxide (TiO_2) has three primary polymorphs: anatase, rutile, and brookite. Tungsten trioxide (WO_3) and manganese dioxide (MnO_2) exist in six different crystal phase, and V_2O_5 itself exists in four diverse crystal phases, which are interchangeable with temperature.[248] Therefore, we limit ourselves to discussing 2D materials that are important for energy storage devices and catalysis, such as V_2O_5, MnO_2, MoO_3, and TiO_2. Binary TMOs, such as V_2O_5 and MoO_3, naturally have a layered crystal structure that can be exfoliated to obtain a 2D structure. As depicted in Figure 1.24, each layer of orthorhombic V_2O_5 comprises a VO_5 square pyramid configuration, which shares sides and corners, and the layers of VO_5 are held by weak vdW forces,[250] and in those layers vanadium and oxygen atoms share a covalent bond. MnO_2, as already mentioned, has a diverse set of structures, which depend on the connectivity between MnO_6 octahedra units *via* sides and corners.[251] Among these,

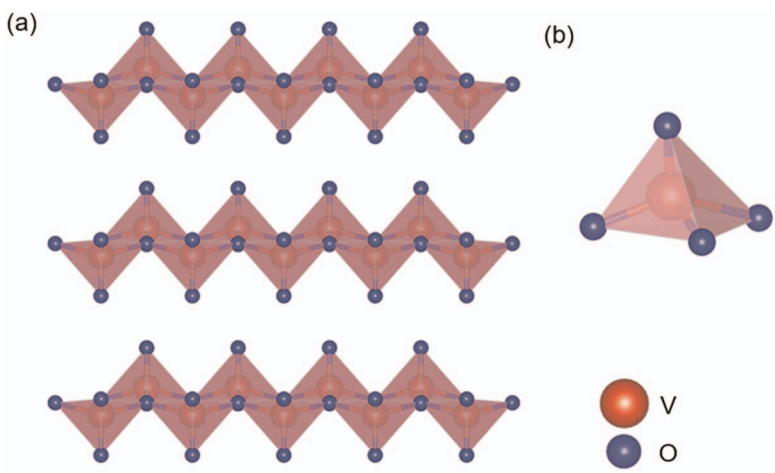

Figure 1.24 (a) Crystal structure of V_2O_5. (b) The square pyramid VO_5 configuration, which is the building unit of V_2O_5.

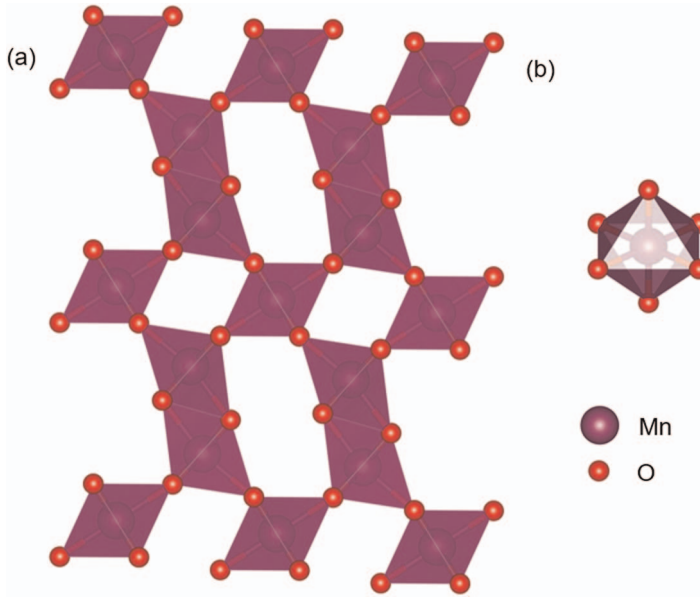

Figure 1.25 (a) Crystal structure of δ-MnO_2 (birnessite) and (b) the octahedral MnO_6 unit, which is the building unit of δ-MnO_2.

δ-MnO_2 (birnessite), as shown in Figure 1.25, is widely used for energy storage applications, owing to its interlayer space, which can accommodate ions such as Li^+, Zn^{2+}, and Al^{3+}. In contrast, its non-layered counterparts, such as α-MnO_2, show extraordinary activity for the OER.

α-MoO_3 is the layered polymorph of MoO_3 and consists of distorted edge-shared MoO_6 octahedral units[252] (see Figure 1.26). Recently, hexagonal (h) phase TiO_2, MnO, Ni_2O_3, *etc.* (Figure 1.27) have been synthesized, and, specifically, mono- and multilayered h-TiO_2 has received more attention. It was reported that h-TiO_2 has a structure similar to MoS_2, with an interlayer spacing of 0.59 nm (from the Ti to Ti distance). High-angle annular dark-field scanning transmission electron microscopy (HAADF-STEM) imaging and DFT calculations showed that the monolayers were stacked in an 'AbA' order, but, surprisingly, the trilayer was stacked in an AA′b configuration.[253]

1.7.2 Optical and Electronic Properties of TMOs

Quantum confinement in 2D layered structures gives rise to interesting electronic and optical properties compared to the bulk counterparts, which can be successfully employed for various applications. For example, bandgap widening (>1 eV) was noticed in thin SnO,[254] whose bulk counterpart has an indirect bandgap of ∼0.7 eV and a direct bandgap of ∼2.7 eV. Interestingly, narrowing of the bandgap was observed in the h-TiO_2 2D layered material;[253] Figure 1.28 shows TiO_2 nanosheets as observed by UV–visible spectroscopy

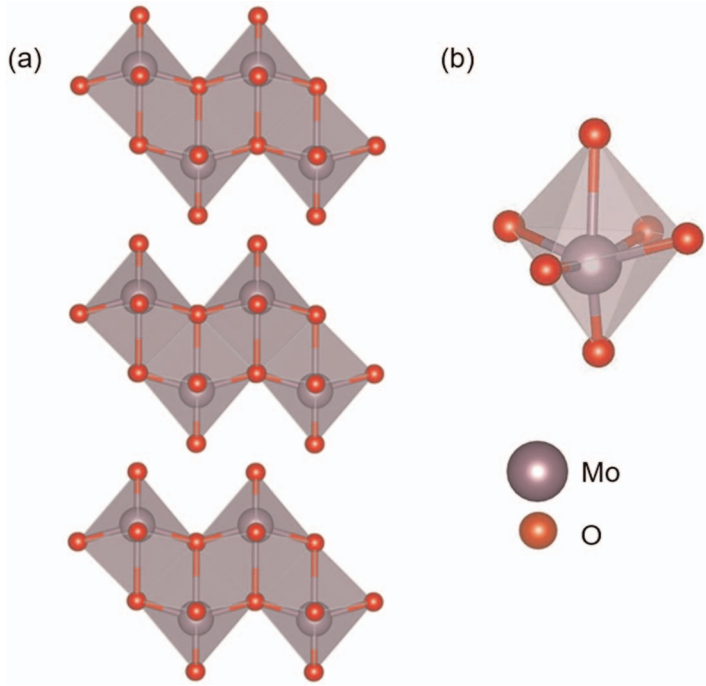

Figure 1.26 (a) Crystal structure of α-MoO_3 and (b) the distorted octahedral MoO_6 unit, which is the building unit of α-MoO_3

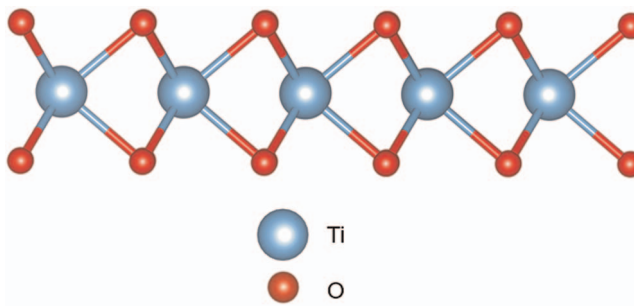

Figure 1.27 Schematic depiction of the monolayer of h-TiO_2.

with their thin dimensions compared to their bulk counterparts. Similarly, the bandgaps of mono-, bi-, and trilayered h-TiO_2 were found to be 2.35, 2.0, and 1.85 eV, respectively, which is less than for anatase (3.2 eV) and rutile (3.0 eV) structures. It has been demonstrated that heteroatom doping has an effect on the lattice structure that gives rise to enhanced electronic and electrochemical properties; similarly to that discussed in the synthesis section.

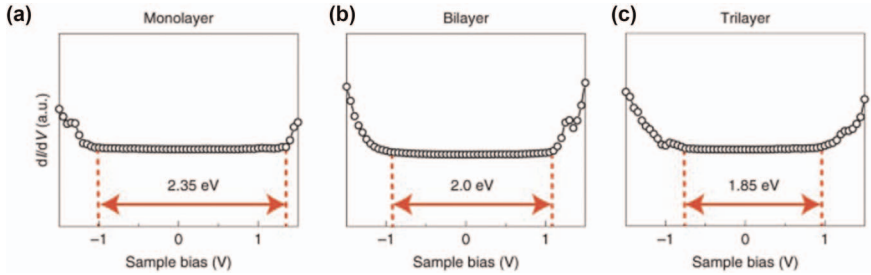

Figure 1.28 Bandgap of (a) monolayer h-TiO_2, (b) bilayer h-TiO_2, and (c) trilayer h-TiO_2.[253] Reproduced from ref. 253 with permission from Springer Nature, Copyright 2021.

1.7.3 Synthesis Routes

Initially, we started by discussing the fact that TMOs fall short in their electronic conductivity; it is particularly vital for materials to have high electronic conductivity when the aim is to use them for energy conversion and energy storage applications. While several strategies are in place to increase the conductivity significantly, it is particularly interesting to discuss these strategies simultaneously with the synthesis techniques. Moreover, tuning the structure while inducing defects can produce more redox-active sites and can simultaneously increase the conductivity. Intrinsically, one can achieve higher conductivity by surface engineering in various ways: (1) inducing metal/oxygen vacancies; (2) initiating lattice strain; (3) introducing heteroatoms into the lattice of the parent structure; and (4) by doping in between the layers. Extrinsically, the conductivity can be increased by hybridization with other conductive materials, such as allotropes of carbon and other 2D TMOs.[248] The synthesis techniques have mainly incorporated these strategies and are discussed in the following sections.

1.7.3.1 Exfoliation

As mentioned previously, synthesizing 2D materials through the Scotch tape method and transferring them to a Si/SiO substrate is a painstakingly difficult task. Not to mention the fact that controlling the lateral dimensions and thickness of the obtained sheets is even more difficult and unpredictable. Therefore, exploring other reasonable and scalable synthesis methods, such as mechanical force-assisted, chemical, and electrochemical exfoliation, is essential. Mechanical exfoliation can be achieved in a batch reactor or a continuous stirred tank (CSTR) reactor employing a high-shear impeller and solvents such as *N*-methyl-2-pyrrolidone (NMP). Work reported by Hua *et al.*[255] (see Figure 1.29) highlighted the use of a CSTR for shape-controlled synthesis of layered $LiNi_{1/3}Co_{1/3}Mn_{1/3}O_2$ and $Li_{1.2}Ni_{0.2}Mn_{0.6}O_2$ materials; and this is an interesting method owing to its ease of scalability. It opens the

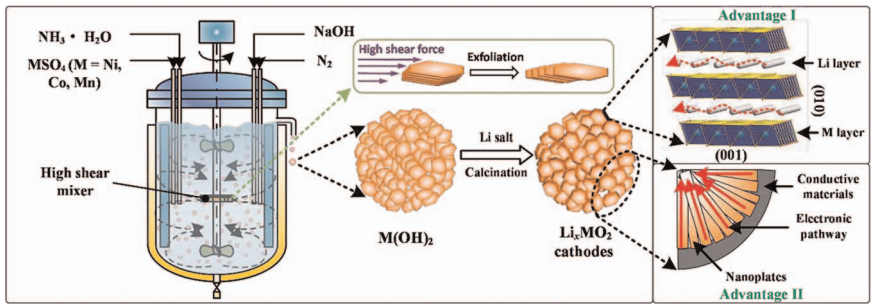

Figure 1.29 Schematic representation of high shear exfoliation in a CSTR.[255] Reproduced from ref. 255 with permission from the Royal Society of Chemistry.

door for large-scale commercial synthesis of other 2D layered materials, as mentioned previously.

As discussed, Zhang *et al.*[253] synthesized hexagonal (h)-phase layered oxides of transition metals, lanthanides, and metalloids. The authors used machine polishing to incorporate nano-level roughness on the metal surface. Following this the metal was placed in a controlled environment for the growth of layered oxide, where the oxygen concentration was adjusted in a way that aligned with the chemisorption energy of the metal. The exfoliated material was subsequently transferred to a Si/SiO_2 substrate. Another method for the synthesis of layered TMOs is the utilization of ultrasound. This is usually used in conjunction with liquid-phase exfoliation, where the ultrasound is used to generate a large number of cavitation bubbles, which, upon implosion, release a huge amount of energy to break the vdW forces existing between the layers, thus leading to the formation of 2D nanosheets. Ultrasound can be generated using an ultrasonic horn (probe sonicator), ultrasonic bath, or a combination of both, to achieve the desired results. Recently, Hanlon *et al.*[256] used the above ultrasound technique to fabricate nanosheets of MoO_3, and Tan *et al.*[257] employed the same strategy to realize V_2O_5 nanosheets.

Various other strategies, such as ion intercalation and exchange-assisted exfoliation, can be employed in liquid-phase exfoliation in conjunction with ultrasound. Depending on the material, there can be a strong interaction between the atomic layers, where ultrasound alone is not enough for facile exfoliation. Hence, additional chemical energy is often required to overcome the strong forces that bind these layers electrostatically. The underlying principle in ion intercalation-assisted exfoliation is the insertion of large molecules into the bulk of the material, thus weakening vdW bonds and causing subsequent layer separation. Rui *et al.*[258] reported the synthesis of ultrathin V_2O_5 nanosheets using this ion-intercalated exfoliation technique. Direct exfoliation of bulk V_2O_5 was achieved in a formamide solvent, as illustrated in Figure 1.30. Here, the formamide solvent is adsorbed into the interlayer space, decreasing the vdW forces. Then, exfoliation is promoted *via* ultrasonication, leading to the formation of V_2O_5 nanosheets.

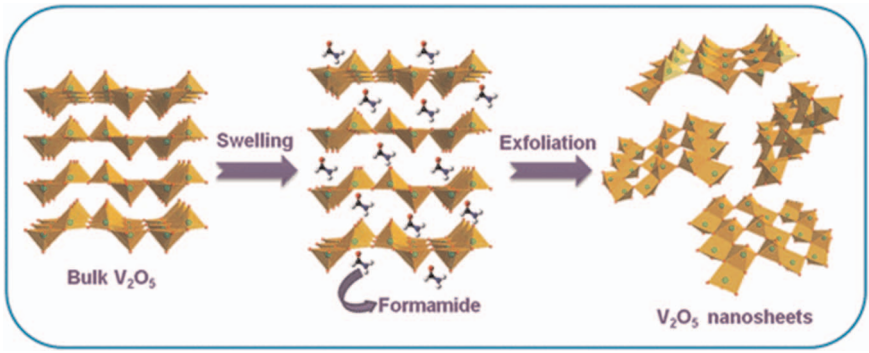

Figure 1.30 Depiction of exfoliation of bulk V_2O_5 using formamide solution.[258] Reproduced from ref. 258 with permission from the Royal Society of Chemistry.

They achieved a few layers of V_2O_5 nanosheets with thicknesses ranging from 2.1 to 3.8 nm and lateral dimensions of 100 to 400 nm. These nanosheets exhibited outstanding electrochemical results; for example, an energy density of 158 W h kg^{-1} at a charge and discharge rate of 50C was achieved when used as a cathode material in LIBs.

1.7.3.2 Hydrothermal Route

Generally, this route is called "hydrothermal" when water is used as a solvent, and when a non-aqueous solvent is involved it is called "solvothermal". The desired results, such as well-defined morphology and lateral size, can be obtained by regulating the reaction parameters, such as temperature and precursor concentration.

Initially, metal salts are used as precursors; they are mixed well in the solvent of choice and are transferred to a Teflon-lined stainless-steel autoclave reactor. Subsequently, the reactor is placed in a hot-air oven, and an appropriate temperature is maintained for a certain period (generally 6–24 h). After heating, the reactor is allowed to cool down naturally to room temperature, and subsequently the precipitates are ultracentrifuged and washed thoroughly with deionized water and ethanol to remove any undesired contaminants. The samples are then dried in a hot-air oven and calcined to obtain the final product.

A variation of the above method using a capping agent was used by Tan *et al.*[259] to synthesize TiO_2 nanosheets using tetramethylammonium hydroxide (TMAH) as a capping agent during the hydrothermal process. It was found that TMAH intercalation was the reason for the formation of nanosheets as the reaction time increased. In addition, a surfactant can also be used in the hydrothermal synthetic technique to obtain 2D nanosheets with the preferred dimensions required for energy storage applications.

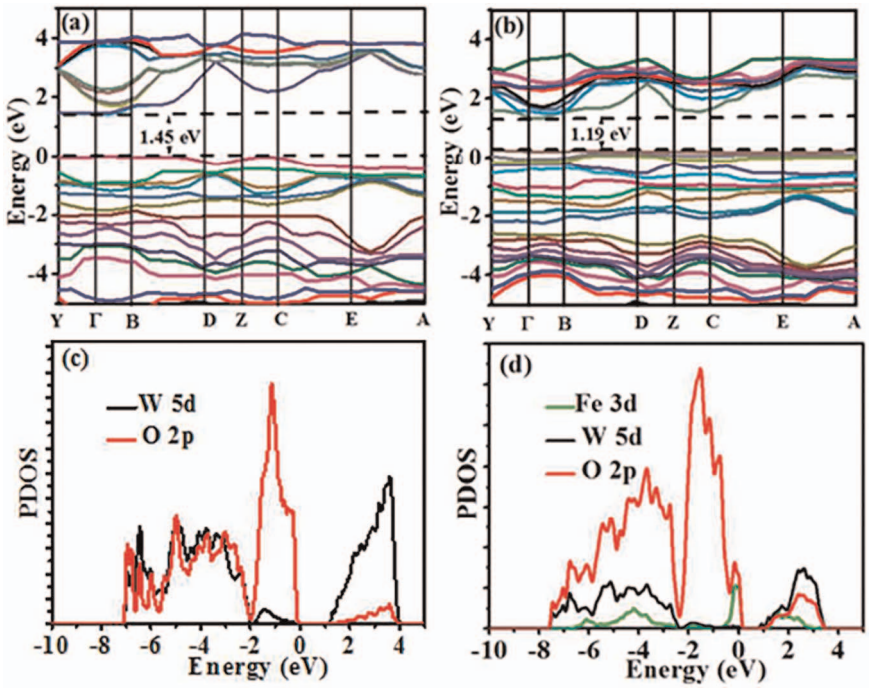

Figure 1.31 (a) The bandgap of pristine WO_3 and (b) the decrease in bandgap of the W-doped WO_3. Comparison of the partial density of states (PDOS) of (c) undoped WO_3 and (d) Fe-doped WO_3.[260] Adapted from ref. 260 with permission from the Royal Society of Chemistry.

Zhang *et al.*[260] have reported the effects of heteroatom incorporation in binary TMO sheets. They successfully synthesized Fe-doped WO_3, which showed a decreased bandgap and exhibited enhanced photoelectrochemical (PEC) performance. The reasons for this were: (1) hybridization within Fe 3d, W 5d, and O 2p orbitals, which led to a downshift in the conduction band by 0.1 eV, owing to interaction of Fe 3d and W 5d; (2) an upshift in the valence band by 0.16 eV brought about by Fe 3d and O 2p interaction, with the combined effect of both the upshift and downshift resulting in a bandgap decrease (see Figure 1.31); and (3) finally, the formation of oxygen vacancies due to Fe doping, with the charge carrier concentration showing an increase from 3.3×10^{19} cm^{-3} for undoped WO_3 to 5.6×10^{21} cm^{-3} for 2% Fe-doped WO_3.

Similarly, Zhang *et al.*[261] investigated the effects of heteroatom incorporation in MoO_3, and they developed a facile hydrothermal synthesis route for H atom intercalation. Although the authors did not use it for energy applications, this study provided a very good idea for H injection. The study highlights that the increase in H^+ ions resulted in greater exfoliation of MoO_3 from the parent structure and eventually formed a 2D nanodisk structure with three different compositions: (1) $H_{0.3}MoO_3$, (2) $H_{0.91}MoO_3$,

and (3) $H_{1.55}MoO_3$. They found a change in band structure with hydrogen incorporation, which led to an increase in the Fermi level. They also noted a transition from semiconductor to metal-like behaviour as the oxidation state of Mo reduced from +6 to +5 and +4 oxidation states, which caused single and double filling of Mo 4d orbitals. Interestingly, there was an increase in the free electron concentration from 5.82×10^{21} per cm^3 for $H_{0.3}MoO_3$ to 1.77×10^{22} per cm^3 for $H_{0.91}MoO_3$ and to 3.01×10^{22} per cm^3 for $H_{1.55}MoO_3$. Additionally, Ju *et al.*[262] evaluated the performance of H_xMoO_3 as an anode in lithium-ion batteries following a similar hydrothermal procedure for the synthesis of 2D H_xMoO_3. It was found that $H_{0.28}MoO_3$ nanobelts exhibited an excellent specific capacity of 920 mA h g^{-1} and maintained a capacity of 550 mA h g^{-1} after 450 cycles at 1 A g^{-1}. Another study on H-doped MoO_3 was conducted by Zou *et al.*[263] Although synthesized using an exfoliation technique, they also showed that H incorporation actually increases the free electron concentration and reduces the bandgap (reduced by 0.2 eV), which potentially opens up this material for various energy applications, such as photocatalytic hydrogen production, electrochemical OER, *etc.*

Shei *et al.*[264] fabricated an asymmetric capacitor using La-doped MoO_3 and V_2O_5@graphene nanosheets as cathode and anode, respectively. These nanosheets were obtained using a hydrothermal technique. Here, heteroatom (La) doping decreases the bandgap of pristine MoO_3 from 2.48 eV to 1.91 eV, thus increasing its electronic conductivity. Further electrochemical studies showed that La-doped MoO_3 has an excellent specific capacitance of 605 F g^{-1} compared to its pristine counterpart, which is just 116.5 F g^{-1}. As for V_2O_5 on graphene nanosheets, it too exhibited a high specific capacitance of 630.8 F g^{-1} compared to its pristine counterpart, which showed a value of 270.8 F g^{-1} at the same current density. The authors used both materials to conduct a complete cell study; their studies found that the device has a very high energy density of 123 W h g^{-1} and a power density of 1000 W kg^{-1}, and, even after 6000 charging-discharging cycles, the capacitance was found to be 95.4% of the initial value. You *et al.*[265] also investigated V_2O_5 nanosheets assembled on carbon fiber felt as a flexible electrode material for asymmetric supercapacitors (a hybrid of both batteries and supercapacitors). The composite exhibited a fairly high capacitance of 492 F g^{-1} and an energy density of 0.928 mW h cm^{-3}, and the material retained 89.7% of its initial capability even after 6000 charging-discharging cycles. Song *et al.*[266] synthesized a Co_3O_4/rGO 2D/2D sheet/sheet nanocomposite using a hydrothermal method and used it as an electrode material for a supercapacitor. This composite exhibited enhanced electrochemical performance due to its higher specific surface area, providing a propensity for exalted storage of ions (insertion/extraction).

1.7.3.3 Self-assembly

Self-assembly is generally a process in which molecules spontaneously arrange themselves in an ordered structure. It is one of the most scalable

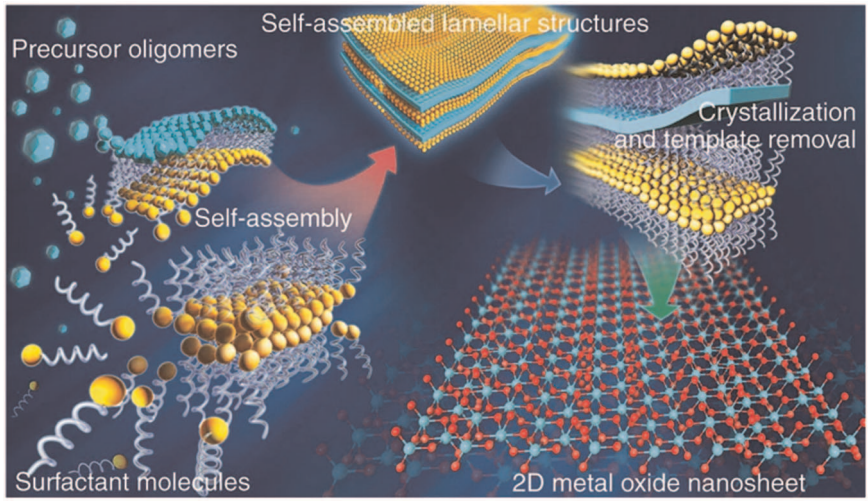

Figure 1.32 Schematic representation of the assembly of 2D TMO NS *via* surfactant-assisted molecular assembly in the liquid phase.[267] Reproduced from ref. 267 with permission from Springer Nature, Copyright 2014.

methods to synthesize 2D nanosheets. This method is particularly interesting as it is often combined with other strategies that have possible drawbacks for producing nanosheets. This technique is usually used for the growth of nanosheets along a desired direction. The general strategy is to employ a surfactant to assist in the assembly, and subsequently to remove the surfactant to achieve ultrathin sheets. Several ultrathin TMOs were synthesized, as demonstrated by Sun *et al.*,[267] using a combination of polyethylene oxide–polypropylene oxide–polyethylene oxide (PEO20–PPO70–PEO20, Pluronic P123) and ethylene glycol (EG) to facilitate self-assembly of transition metal precursors, which resided inside the inverse lamellar micelles, thereby assisting in the formation of TMO layers, as shown in Figure 1.32. The reported role of P123 was to restrict the agglomeration of TMOs, and EG acted as both a co-solvent and co-surfactant, which enabled inverse micelle formation and caused effective separation, leading to the formation of nanosheets.

1.8 Hexagonal Boron Nitride

Boron nitride (BN) is a layered compound that is isoelectronic and isostructural with graphite. BN exits both in amorphous (a-BN) and crystalline structures. The various predominant crystalline structures of BN are cubic boron nitride (c-BN), wurtzite boron nitride (w-BN), and h-BN, as shown in Figure 1.33. Among these, h-BN displays a crystal structure akin to that of graphite.

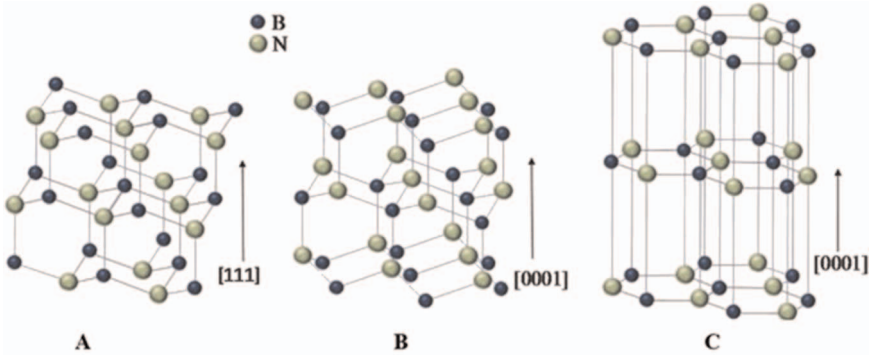

Figure 1.33 Crystal structures of (A) cubic, (B) wurtzite, and (C) hexagonal BN.[297] Reproduced from ref. 297 with permission from John Wiley & Sons, Copyright © 2017 WILEY-VCH Verlag GmbH & Co. KGaA, Weinheim.

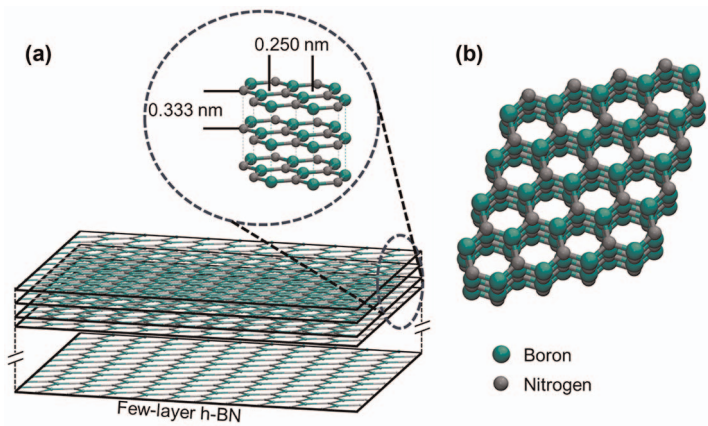

Figure 1.34 (a) The structure of h-BN nanosheets. (b) The lattice of h-BN with an AAA stacking, in which the boron and nitrogen atoms are stacked on each other alternately.

1.8.1 Structure of 2D h-BN

Hexagonal boron nitride is a white powder, in which all the boron and nitrogen atoms are covalently bonded to each other to form 2D monolayers, and these layers are held together by vdW forces, as shown in Figure 1.34a. The B–N bond length is 0.145 nm, the distance between two centre points of adjacent hexagonal rings is 0.25 nm, and the interplanar distance is 0.333 nm, as shown in Figure 1.34a. To satisfy the polar–polar interactions, 2D layers of h-BN layers are stacked in an AA stacking configuration, where B and N atoms of hexagonal rings are superimposed alternately located along the *c* axis, as shown in Figure 1.34b. In contrast, graphite has an AB stacking sequence, where every second alternative layer is shifted in such a way that

carbon atoms in the B layer are exactly above the centre of the hexagonal ring of the A layer, as shown in Figure 1.34a.[268,269]

1.8.2 Properties of h-BN

Hexagonal BN exhibits excellent characteristics of electrical insulation, optical, thermal, and mechanical properties. These properties make 2D h-BN a promising candidate for many applications. The most important properties of 2D h-BN are discussed briefly here.

1.8.2.1 Electronic Properties of h-BN

h-BN is an insulator with a wide bandgap of ~6 eV due to the large electronegativity difference between B and N. As a result, it frequently finds application as a tunnelling dielectric barrier in 2D electronic devices.[270]

1.8.2.2 Mechanical Properties

The Young's modulus of single-layer h-BN estimated by DFT is 0.716–0.977 TPa.[271] The experimental Young's modulus value varies due to changes in the morphology, the number of layers, and defects. Falin *et al.*[272] measured the Young's modulus of graphene and h-BN with increasing numbers of layers, from 1 to 8, using atomic force microscopy. They found that the Young's modulus reduced slightly (1.026 to 0.942 TPa) for graphene and did not change (0.865 TPa) for h-BN with increasing numbers of layers.

1.8.2.3 Thermal Properties

The strong bond between B and N in h-BN makes it a thermally stable material at high temperatures. Most importantly, it decomposes at 1000 °C in air, at 1400 °C in vacuum, and at 2800 °C in an inert atmosphere.[273,274] The in-planar and bulk thermal conductivities estimated by Zhang *et al.*[275] are 600 $W m^{-1} K^{-1}$ and 400 $W m^{-1} K^{-1}$, respectively. Due to its stability at high temperatures and low thermal conductivity, h-BN can be used as an effective insulating material.

1.8.3 Applications of h-BN

1.8.3.1 Substrates for Graphene Electronics

Generally, graphene-based devices, such as photodetectors, solar cells, *etc.*, are fabricated using silica (SiO_2) as the substrate material. However, deposition of graphene on the SiO_2 substrate causes some restrictions on the architecture and performance of the device. An alternative for graphene as a substrate material is 2D h-BN, as it has a similar lattice constant, is free of charge traps and dangling bonds, and has a large bandgap.[276,277] Lee *et al.*[278]

prepared h-BN nanosheets by CVD and used it as a substrate, along with silica, in graphene-based thin film transistors. The performance of transistors with h-BN nanosheets increased by three times compared to those without h-BN.

1.8.3.2 Dielectric Material

So far, SiO_2, HfO_2, Al_2O_3, *etc.* have been used as dielectric materials in electronic devices. However, they have some drawbacks, such as current leakage, failure at higher voltage, *etc.* The use of 2D insulating materials, such as h-BN nanosheets, helps us to overcome these drawbacks, due to the exceptional properties of the 2D material. 2D h-BN nanosheets are proven to be excellent dielectric materials in graphene and molybdenum disulfide (MoS_2) and other 2D nanomaterial-based electronic devices.[277,279,280] For example, Shi *et al.*[281] fabricated nanocapacitors using h-BN as the dialectic material. They found that h-BN performed exceptionally well; when the thickness of the h-BN layer was less than 5 nm, the capacitance increased more than 100%.

1.8.3.3 Tunnelling Barrier

h-BN has a low out-of-plane dielectric constant (k) in the range 3.29 to 3.76 (thickness dependent), and the in-plane constant is in the range 6.82 to 6.93.[282] The bandgap of h-BN is larger than 6 eV, so it acts as an electrical insulator. This makes h-BN a potential tunnelling barrier in electronic devices. 2D h-BN nanosheets are stable against voltage stress, thus overcoming the challenges of conventional dielectrics, such as charge trapping, current leakage, and dielectric breakdown.[283] Britnell *et al.*[284] studied the electronic properties of ultrathin h-BN layers prepared by a micromechanical cleavage technique with conducting materials (graphene, graphite, and gold) on both sides. They found that h-BN acted as an excellent tunnelling barrier.

1.8.3.4 Protecting and Passivating Layer

The special characteristics of h-BN, such as thermal stability up to 850 °C, electrical insulation, and chemical inertness, make it a perfect material for use as a protecting layer. Degradation of the materials in electric devices can be prevented by using an h-BN coating. For example, Chilkoor *et al.*[285] used a thin layer of h-BN as an insulating barrier for microbial-induced corrosion by *Desulfovibrio alaskensis* G20 bacteria on copper. They found that a single layer of h-BN acted as a barrier and showed 91% efficiency in preventing aggressive metabolites, which is on a par with that of commercial thick coatings.

1.8.3.5 Sensors

h-BN has been used in sensors for the detection of different compounds (ethanol, NH_3, NO_2, NO, *etc.*) in low concentration (at ppm levels).[286] When

gases/chemicals are adsorbed onto the surface of h-BN there is change in the conductance, which can be measured. Raad *et al.*[287] investigated the graphene/h-BN multiheterostructure for sensing of H_2O, NH_3, and NO_2. It was found that the structure was sensitive to NH_3 and NO_2. Khan *et al.*[288] investigated 2D h-BN nanosheets for electrochemical sensing of dopamine.

1.8.3.6 Catalysis

h-BN nanosheets have been used as potential catalysts for many chemical reactions, as it is possible to produce different vacancies in the 2D sheets of h-BN, with both nitrogen and boron vacancies being possible. These vacancies in h-BN nanosheets can be converted to active sites, by embedding carbon (C) and other metal atoms for multiple reactions. Various metal atoms (Co, Fe, Pt, Ag, Au, *etc.*) and C embedded in the vacancies of h-BN have been studied.[289] Marbaniang *et al.*[290] prepared carbon-doped h-BN using CVD and used it as an electrocatalyst for the oxygen reduction reaction. Interestingly, carbon-doped h-BN showed good catalytic activity.

1.8.4 Synthesis Methods of h-BN

The properties of 2D h-BN nanosheets, such as electric, optical, thermal, mechanical, *etc.*, depend on the quality of the 2D h-BN nanosheets, which is in turn determined by the synthesis method. Like the other 2D families, h-BN is realized through top-down (mechanical cleavage, liquid exfoliation, modified Hummers' method) and bottom-up (CVD, pulsed laser deposition, physical vapor deposition, *etc.*) synthesis methods. The details of these production methods can be found in comprehensive reviews.[291]

1.9 Conclusion

Graphene created a revolution in the field of 2D materials due to its exceptional combination of properties. However, limitations concerning its real-world implementation have paved the way for the discovery and development of many similar and innovative 2D nanomaterials. This chapter has delved into the structure, properties, applications, and synthesis techniques of various cutting-edge 2D nanomaterials, including TMDs, MXenes, TMOs, and h-BN. These materials exhibit unique characteristics and diverse applications, offering promising avenues for sustainable energy solutions, from energy storage to catalysis.

In conclusion, the rapid advancement of these nanomaterials presents a promising pathway to achieve sustainable energy solutions. However, addressing challenges related to large-scale manufacturing techniques, fabrication and engineering limitations, and high cost remains crucial to realizing the full potential of nanomaterial-based technologies. By continuing to explore and innovate in fields such as chemical engineering and

materials science, we can overcome these obstacles and accelerate the transition towards a cleaner and more sustainable energy future.

References

1. N. Baig, *Composites, Part A*, 2023, **165**, 107362.
2. A. K. Geim and K. S. Novoselov, *Nat. Mater.*, 2007, **6**, 183–191.
3. C. Ataca, H. Şahin and S. Ciraci, *J. Phys. Chem. C*, 2012, **116**, 8983–8999.
4. S. Stankovich, D. A. Dikin, G. H. B. Dommett, K. M. Kohlhaas, E. J. Zimney, E. A. Stach, R. D. Piner, S. B. T. Nguyen and R. S. Ruoff, *Nature*, 2006, **442**, 282–286.
5. K. S. Novoselov, A. K. Geim, S. V. Morozov, D. Jiang, Y. Zhang, S. V. Dubonos, I. V. Grigorieva and A. A. Firsov, *Electric Field Effect in Atomically Thin Carbon Films*, Kluwer, 2004, vol. 404.
6. H. Zhang, *ACS Nano*, 2015, **9**, 9451–9469.
7. M. Xu, T. Liang, M. Shi and H. Chen, *Chem. Rev.*, 2013, **113**, 3766–3798.
8. A. N. Sidorov, M. M. Yazdanpanah, R. Jalilian, P. J. Ouseph, R. W. Cohn and G. U. Sumanasekera, *Nanotechnology*, 2007, **18**, 135301.
9. Ö. Güler and N. Bağcı, *J. Mater. Res. Technol.*, 2020, **9**, 6808–6833.
10. Y. Yang, C. Han, B. Jiang, J. Iocozzia, C. He, D. Shi, T. Jiang and Z. Lin, *Mater. Sci. Eng., R*, 2016, **102**, 1–72.
11. A. A. Balandin, S. Ghosh, W. Bao, I. Calizo, D. Teweldebrhan, F. Miao and C. N. Lau, *Nano Lett.*, 2008, **8**, 902–907.
12. S. Syama and P. V. Mohanan, *Int. J. Biol. Macromol.*, 2016, **86**, 546–555.
13. C. Lee, X. Wei, J. W. Kysar and J. Hone, *Science*, 2008, **321**, 385–388.
14. C. N. R. Rao, A. K. Sood, K. S. Subrahmanyam and A. Govindaraj, *Angew. Chem., Int. Ed.*, 2009, **48**, 7752–7777.
15. V. B. Mbayachi, E. Ndayiragije, T. Sammani, S. Taj, E. R. Mbuta and A. U. Khan, *Results Chem.*, 2021, **3**, 100163.
16. K. S. Novoselov, *Science*, 2004, **306**, 666–669.
17. M. J. Allen, V. C. Tung and R. B. Kaner, *Chem. Rev.*, 2010, **110**, 132–145.
18. W. S. Hummers and R. E. Offeman, *J. Am. Chem. Soc.*, 1958, **80**, 1339.
19. G. Xin, W. Hwang, N. Kim, S. M. Cho and H. Chae, *Nanotechnology*, 2010, **21**, 405201.
20. D. V. Kosynkin, A. L. Higginbotham, A. Sinitskii, J. R. Lomeda, A. Dimiev, B. K. Price and J. M. Tour, *Nature*, 2009, **458**, 872–876.
21. L. Jiao, X. Wang, G. Diankov, H. Wang and H. Dai, *Nat. Nanotechnol.*, 2010, **5**, 321–325.
22. S. Thakur and N. Karak, *Carbon*, 2012, **50**, 5331–5339.
23. S. Pei and H.-M. Cheng, *Carbon*, 2012, **50**, 3210–3228.
24. S. Y. Toh, K. S. Loh, S. K. Kamarudin, W. Ramli and W. Daud, DOI: 10.1016/j.cej.2014.04.004.
25. S. Park, J. An, J. R. Potts, A. Velamakanni, S. Murali and R. S. Ruoff, *Carbon*, 2011, **49**, 3019–3023.

26. A. Reina, X. Jia, J. Ho, D. Nezich, H. Son, V. Bulovic, M. S. Dresselhaus and J. Kong, *Nano Lett.*, 2009, **9**, 30–35.
27. W. A. de Heer, C. Berger, X. Wu, P. N. First, E. H. Conrad, X. Li, T. Li, M. Sprinkle, J. Hass, M. L. Sadowski, M. Potemski and G. Martinez, *Solid State Commun.*, 2007, **143**, 92–100.
28. D. G. Papageorgiou, I. A. Kinloch and R. J. Young, *Prog. Mater. Sci.*, 2017, **90**, 75–127.
29. C. N. R. Rao, U. Maitra and H. S. S. R. Matte, in *Graphene*, Wiley-VCH Verlag GmbH & Co. KGaA, Weinheim, Germany, 2012, pp. 1–47.
30. K. R. Paton, E. Varrla, C. Backes, R. J. Smith, U. Khan, A. O'Neill, C. Boland, M. Lotya, O. M. Istrate, P. King, T. Higgins, S. Barwich, P. May, P. Puczkarski, I. Ahmed, M. Moebius, H. Pettersson, E. Long, J. Coelho, S. E. O'Brien, E. K. McGuire, B. M. Sanchez, G. S. Duesberg, N. McEvoy, T. J. Pennycook, C. Downing, A. Crossley, V. Nicolosi and J. N. Coleman, *Nat. Mater.*, 2014, **13**, 624–630.
31. Z. Lin, P. Karthik, M. Hada, T. Nishikawa and Y. Hayashi, *Nanomaterials*, 2017, **7**, 125.
32. K. R. Paton, E. Varrla, C. Backes, R. J. Smith, U. Khan, A. O'Neill, C. Boland, M. Lotya, O. M. Istrate, P. King, T. Higgins, S. Barwich, P. May, P. Puczkarski, I. Ahmed, M. Moebius, H. Pettersson, E. Long, J. Coelho, S. E. O'Brien, E. K. McGuire, B. M. Sanchez, G. S. Duesberg, N. McEvoy, T. J. Pennycook, C. Downing, A. Crossley, V. Nicolosi and J. N. Coleman, *Nat. Mater.*, 2014, **13**, 624–630.
33. A. S. Pavlova, E. A. Obraztsova, A. V. Belkin, C. Monat, P. Rojo-Romeo and E. D. Obraztsova, *J. Nanophotonics*, 2016, **10**, 12525.
34. W. S. Hummers and R. E. Offeman, *J. Am. Chem. Soc.*, 1958, **80**, 1339.
35. L. Staudenmaier, *Ber. Dtsch. Chem. Ges.*, 1898, **31**, 1481–1487.
36. Y. Wu, T. Yu and Z. Shen, *J. Appl. Phys.*, 2010, **108**, 71301.
37. D. R. Dreyer, S. Park, C. W. Bielawski and R. S. Ruoff, *Chem. Soc. Rev.*, 2009, **39**, 228–240.
38. M. S. A. Bhuyan, M. N. Uddin, M. M. Islam, F. A. Bipasha and S. S. Hossain, *Int. Nano Lett.*, 2016, **6**, 65–83.
39. A. T. Hoang, L. Hu, A. K. Katiyar and J. H. Ahn, *Matter*, 2022, **5**, 4116–4132.
40. D. Wei, B. Wu, Y. Guo, G. Yu and Y. Liu, *Acc. Chem. Res.*, 2013, **46**, 106–115.
41. K. E. Whitener and P. E. Sheehan, *Diamond Relat. Mater.*, 2014, **46**, 25–34.
42. G. Yazdi, T. Iakimov and R. Yakimova, *Crystals*, 2016, **6**, 53.
43. R. F. Davis, G. Kelner, M. Shur, J. W. Palmour and J. A. Edmond, *Proc. IEEE*, 1991, **79**, 677–701.
44. S. Niyogi, E. Bekyarova, M. E. Itkis, J. L. McWilliams, M. A. Hamon and R. C. Haddon, *J. Am. Chem. Soc.*, 2006, **128**, 7720–7721.
45. Y. Zhu, S. Murali, W. Cai, X. Li, J. W. Suk, J. R. Potts and R. S. Ruoff, *Adv. Mater.*, 2010, **22**, 3906–3924.

46. S. Obata, K. Saiki, T. Taniguchi, T. Ihara, Y. Kitamura and Y. Matsumoto, *J. Phys. Soc. Jpn.*, 2015, **84**, 121012.
47. R. Xing, Y. Li and H. Yu, *Chem. Commun.*, 2016, **52**, 390–393.
48. D. A. Dikin, S. Stankovich, E. J. Zimney, R. D. Piner, G. H. B. Dommett, G. Evmenenko, S. T. Nguyen and R. S. Ruoff, *Nature*, 2007, **448**, 457–460.
49. I. V. Lightcap and P. V. Kamat, *Acc. Chem. Res.*, 2013, **46**, 2235–2243.
50. X. Sun, Z. Liu, K. Welsher, J. T. Robinson, A. Goodwin, S. Zaric and H. Dai, *Nano Res.*, 2008, **1**, 203–212.
51. C. Chung, Y.-K. Kim, D. Shin, S.-R. Ryoo, B. H. Hong and D.-H. Min, *Acc. Chem. Res.*, 2013, **46**, 2211–2224.
52. C. Gómez-Navarro, M. Burghard and K. Kern, *Nano Lett.*, 2008, **8**, 2045–2049.
53. T. Cheng-an, Z. Hao, W. Fang, Z. Hui, Z. Xiaorong and W. Jianfang, *Polym. Polym. Compos.*, 2017, **25**, 11–16.
54. S. Jiang, Z. He, Q. Li, J. Wang, G. Wu, Y. Zhao and M. Kang, *Polym. Compos.*, 2019, **40**, E953–E961.
55. D. J. Prasanna Kumar, S. Verma, K. Jasuja and P. Dayal, *Phys. Chem. Chem. Phys.*, 2019, **21**, 3164–3173.
56. D. J. P. Kumar, K. R. Reddy and P. Dayal, *Phys. Chem. Chem. Phys.*, 2020, **22**, 24516–24525.
57. D. J. P. Kumar, C. Borkar and P. Dayal, *Langmuir*, 2021, **37**, 12586–12595.
58. M. Kim, C. Lee, Y. D. Seo, S. Cho, J. Kim, G. Lee, Y. K. Kim and J. Jang, *Chem. Mater.*, 2015, **27**, 6238–6248.
59. A. Hunt, E. Z. Kurmaev and A. Moewes, *Carbon*, 2014, **75**, 366–371.
60. D. Voiry, J. Yang, J. Kupferberg, R. Fullon, C. Lee, H. Y. Jeong, H. S. Shin and M. Chhowalla, *Science*, 2016, **353**, 1413–1416.
61. P. Kumar, F. Shahzad, S. Yu, S. M. Hong, Y.-H. Kim and C. M. Koo, *Carbon*, 2015, **94**, 494–500.
62. L. L. Zhang, X. Zhao, M. D. Stoller, Y. Zhu, H. Ji, S. Murali, Y. Wu, S. Perales, B. Clevenger and R. S. Ruoff, *Nano Lett.*, 2012, **12**, 1806–1812.
63. M. Kim, C. Lee and J. Jang, *Adv. Funct. Mater.*, 2014, **24**, 2489–2499.
64. C. B. in Kim, J. Lee, J. Cho and M. Goh, *Carbon*, 2018, **139**, 386–392.
65. J. Kim, H. Im, J. Kim and J. Kim, *J. Mater. Sci.*, 2012, **47**, 1418–1426.
66. A. T. Smith, A. M. LaChance, S. Zeng, B. Liu and L. Sun, *Nano Mater. Sci.*, 2019, **1**, 31–47.
67. P. K. Singh and P. Kumar Singh, *Mod. Phys. Lett. B*, 2023, **38**, 2450014.
68. D. G. Trikkaliotis, A. K. Christoforidis, A. C. Mitropoulos and G. Z. Kyzas, *ChemEngineering*, 2021, **5**, 64.
69. J. Zhang, H. Yang, G. Shen, P. Cheng, J. Zhang and S. Guo, *Chem. Commun.*, 2010, **46**, 1112–1114.
70. K. Maeda, X. Wang, Y. Nishihara, D. Lu, M. Antonietti and K. Domen, *J. Phys. Chem. C*, 2009, **113**, 4940–4947.

71. P. R. Anusuyadevi and A. J. Svagan, in *Nanostructured Photocatalysts*, ed. V.-H. Nguyen, D.-V. N. Vo and S. B. T.-N. P. Nanda, Elsevier, 2021, pp. 305–330.
72. C. Xu, P. Ravi Anusuyadevi, C. Aymonier, R. Luque and S. Marre, *Chem. Soc. Rev.*, 2019, **48**, 3868–3902.
73. W.-J. Ong, L.-L. Tan, Y. H. Ng, S.-T. Yong and S.-P. Chai, *Chem. Rev.*, 2016, **116**, 7159–7329.
74. Q. Han, B. Wang, J. Gao, Z. Cheng, Y. Zhao, Z. Zhang and L. Qu, *ACS Nano*, 2016, **10**, 2745–2751.
75. J. Zhu, P. Xiao, H. Li and S. A. C. Carabineiro, *ACS Appl. Mater. Interfaces*, 2014, **6**, 16449–16465.
76. F. Su, M. Antonietti and X. Wang, *Catal. Sci. Technol.*, 2012, **2**, 1005–1009.
77. T. Fidan, M. Torabfam, Q. Saleem, C. Wang, H. Kurt, M. Yüce, J. Tang and M. K. Bayazit, *Adv. Energy Sustainability Res.*, 2021, **2**, 2000073.
78. Q. Su, J. Sun, J. Wang, Z. Yang, W. Cheng and S. Zhang, *Catal. Sci. Technol.*, 2014, **4**, 1556.
79. W. Zhao, Z. Yan and L. Qian, *Eng. Sci.*, 2020, **10**, 24–34.
80. J. Tian, Q. Liu, A. M. Asiri, A. O. Al-Youbi and X. Sun, *Anal. Chem.*, 2013, **85**, 5595–5599.
81. X. Zhang, X. Xie, H. Wang, J. Zhang, B. Pan and Y. Xie, *J. Am. Chem. Soc.*, 2013, **135**, 18–21.
82. X. Wang, K. Maeda, A. Thomas, K. Takanabe, G. Xin, J. M. Carlsson, K. Domen and M. Antonietti, *Nat. Mater.*, 2009, **8**, 76–80.
83. S. C. Yan, Z. S. Li and Z. G. Zou, *Langmuir*, 2009, **25**, 10397–10401.
84. Y. Wang, X. Wang and M. Antonietti, *Angew. Chem., Int. Ed.*, 2012, **51**, 68–89.
85. Y. Zhang, A. Thomas, M. Antonietti and X. Wang, *J. Am. Chem. Soc.*, 2009, **131**, 50–51.
86. Q. Zhu, Z. Xu, B. Qiu, M. Xing and J. Zhang, *Small*, 2021, **17**, 2101070.
87. Y. Cui, X. Sheng, R. Anusuyadevi, M. Lawoko and A. J. Svagan, *Carbon Trends*, 2021, **3**, 40.
88. A. Thomas, F. Goettmann and M. Antonietti, *Chem. Mater.*, 2008, **20**, 738–755.
89. Y. Fukasawa, K. Takanabe, A. Shimojima, M. Antonietti, K. Domen and T. Okubo, *Chem. – Asian J.*, 2010, **6**, 103–109.
90. S. N. Talapaneni, G. P. Mane, A. Mano, C. Anand, D. S. Dhawale, T. Mori and A. Vinu, *ChemSusChem*, 2012, **5**, 700–708.
91. Y. Zheng, J. Liu, J. Liang, M. Jaroniec and S. Z. Qiao, *Energy Environ. Sci.*, 2012, **5**, 6717–6731.
92. H. Yan, *Chem. Commun.*, 2012, **48**, 3430–3432.
93. M. Tahir, C. Cao, F. K. Butt, A. Mahmood, F. Idrees, S. Hussain, M. Tanveer, Z. Ali and I. Aslam, *ACS Appl. Mater. Interfaces*, 2014, **6**, 1258–1265.
94. Q. Yu, S. Guo, X. Li and M. Zhang, *Mater. Technol.*, 2014, **29**, 172–178.

95. J. Fu, J. Yu, C. Jiang and B. Cheng, *Adv. Energy Mater.*, 2018, 8.
96. M. Dvorak, W. Oswald and Z. Wu, *Sci. Rep.*, 2013, **3**, 2289.
97. J. L. Suter and P. V. Coveney, *Sci. Rep.*, 2021, **11**, 22460.
98. R. H. J. Vervuurt, B. Karasulu, N. F. W. Thissen, Y. Jiao, J. W. Weber, W. M. M. Kessels and A. A. Bol, *Adv. Mater. Interfaces*, 2018, **5**, 1800268.
99. X. J. Lee, B. Y. Z. Hiew, K. C. Lai, L. Y. Lee, S. Gan, S. Thangalazhy-Gopakumar and S. Rigby, *J. Taiwan Inst. Chem. Eng.*, 2019, **98**, 163–180.
100. C. Prasad, H. Tang, Q. Liu, I. Bahadur, S. Karlapudi and Y. Jiang, *Int. J. Hydrogen Energy*, 2020, **45**, 337–379.
101. M. Chhowalla, H. S. Shin, G. Eda, L. J. Li, K. P. Loh and H. Zhang, *Nat. Chem.*, 2013, **5**, 263–275.
102. T. Rao, H. Wang, Y. Zeng, Z. Guo, H. Zhang and W. Liao, *Adv. Sci.*, 2021, **8**, 2002284.
103. X. Li, X. Shi, D. Marian, D. Soriano, T. Cusati, G. Iannaccone, G. Fiori, Q. Guo, W. Zhao and Y. Wu, *Sci. Adv.*, 2023, **9**, 1–8.
104. B. Zhao, D. Shen, Z. Zhang, P. Lu, M. Hossain, J. Li, B. Li and X. Duan, *Adv. Funct. Mater.*, 2021, **31**, 1–36.
105. J. Wang, F. Cheng, Y. Sun, H. Xu and L. Cao, *Phys. Chem. Chem. Phys.*, 2024, **26**, 7988–8012.
106. Z. Qian, L. Jiao and L. Xie, *Chin. J. Chem.*, 2020, **38**, 753–760.
107. W. Zhao, R. M. Ribeiro and G. Eda, *Acc. Chem. Res.*, 2015, **48**, 91–99.
108. Z. Zhang, P. Yang, M. Hong, S. Jiang, G. Zhao, J. Shi, Q. Xie and Y. Zhang, *Nanotechnology*, 2019, **30**, 18.
109. J. H. Kim, H. Sung and G. H. Lee, *Small Sci.*, 2024, **4**, 2300093.
110. G. Wang, Y. Zhang, H. S. Cho, X. Zhao, F. Kim and J. Zou, *ACS Appl. Energy Mater.*, 2021, **4**, 14180–14190.
111. Q. Huang, X. Li, M. Sun, L. Zhang, C. Song, L. Zhu, P. Chen, Z. Xu, W. Wang and X. Bai, *Adv. Mater. Interfaces*, 2017, **4**, 1–6.
112. Y. C. Lin, D. O. Dumcenco, Y. S. Huang and K. Suenaga, *Nat. Nanotechnol.*, 2014, **9**, 391–396.
113. L. A. H. Jones, Z. Xing, J. E. N. Swallow, H. Shiel, T. J. Featherstone, M. J. Smiles, N. Fleck, P. K. Thakur, T. L. Lee, L. J. Hardwick, D. O. Scanlon, A. Regoutz, T. D. Veal and V. R. Dhanak, *J. Phys. Chem. C*, 2022, **126**, 21022–21033.
114. J. Kang, S. Tongay, J. Zhou, J. Li and J. Wu, *Appl. Phys. Lett.*, 2013, **102**(1), 012111.
115. E. Llobet, *Curr. Opin. Environ. Sci. Health*, 2024, **37**, 100533.
116. C. Zhang, C. Gong, Y. Nie, K.-A. Min, C. Liang, Y. J. Oh, H. Zhang, W. Wang, S. Hong, L. Colombo, R. M. Wallace and K. Cho, *2D Mater.*, 2016, **4**, 015026.
117. A. Rahman, J. R. Jennings, A. L. Tan and M. M. Khan, *ACS Omega*, 2022, **7**, 22089–22110.
118. T. Manyepedza, T. Auvray, T. Friščić and N. V. Rees, *Electrochemcommun*, 2024, **160**, 107678.

119. Z. Zhu, A. Mosallanezhad, D. Sun, X. Lei, X. Liu, Z. Pei, G. Wang and Y. Qian, *Energy Fuels*, 2021, **35**, 5613–5626.
120. Q. Xia, L. Zhao, D. Li, J. Wang, L. Liu, C. Hou, X. Liu, H. Xu, F. Dang and J. Zhang, *J. Mater. Chem. A*, 2021, **9**, 19922–19931.
121. S. Jun, J.-W. Lee, S.-C. Kim, S. J. Oh and S. Jeong, *J. Mater. Chem. A*, 2024, **12**, 7522–7527.
122. J. N. Coleman, M. Lotya, A. O'neill, S. D. Bergin, P. J. King, U. Khan, K. Young, A. Gaucher, S. De, R. J. Smith, I. V. Shvets, S. K. Arora, G. Stanton, H.-Y. Kim, K. Lee, G. T. Kim, G. S. Duesberg, T. Hallam, J. J. Boland, J. J. Wang, J. F. Donegan, J. C. Grunlan, G. Moriarty, A. Shmeliov, R. J. Nicholls, J. M. Perkins, E. M. Grieveson, K. Theuwissen, D. W. Mccomb, P. D. Nellist and V. Nicolosi, Two-Dimensional Nanosheets Produced by Liquid Exfoliation of Layered Materials, *Science*, 2011, **331**, 568–571.
123. M. Kulichenko and A. I. Boldyrev, *J. Phys. Chem. C*, 2020, **124**, 6267–6273.
124. X. Hu, L. Yan, L. Ding, N. Zheng, D. Li, T. Ji, N. Chen and J. Hu, *Coord. Chem. Rev.*, 2024, **499**, 215504.
125. Z. Y. Zhu, Y. C. Cheng and U. Schwingenschlögl, *Phys. Rev. B: Condens. Matter Mater. Phys.*, 2011, **84**, 153402.
126. A. Kormányos, G. Burkard, M. Gmitra, J. Fabian, V. Zólyomi, N. D. Drummond and V. Fal'Ko, *2D Mater.*, 2015, **2**, 022001.
127. D. Xiao, G. B. Liu, W. Feng, X. Xu and W. Yao, *Phys. Rev. Lett.*, 2012, **108**, 196802.
128. J. Kim, C. Jin, B. Chen, H. Cai, T. Zhao, P. Lee, S. Kahn, K. Watanabe, T. Taniguchi, S. Tongay, M. F. Crommie and F. Wang, *Sci. Adv.*, 2017, **3**, 1–6.
129. S. A. Vitale, D. Nezich, J. O. Varghese, P. Kim, N. Gedik, P. Jarillo-Herrero, D. Xiao and M. Rothschild, *Small*, 2018, **14**, e1801483.
130. E. C. Ahn, *npj 2D Mater. Appl.*, 2020, **4**, 17.
131. Y. Liu, Y. Li, F. Peng, Y. Lin, S. Yang, S. Zhang, H. Wang, Y. Cao and H. Yu, *Appl. Catal., B*, 2019, **241**, 236–245.
132. R. Shanker, P. Ravi Anusuyadevi, S. Gamage, T. Hallberg, H. Kariis, D. Banerjee, A. J. Svagan and M. P. Jonsson, *ACS Nano*, 2022, **16**, 10156–10162.
133. P. R. Anusuyadevi, S. Singha, D. Banerjee, M. P. Jonsson, M. S. Hedenqvist and A. J. Svagan, *Adv. Mater. Interfaces*, 2023, **10**, 2202112.
134. P. R. Anusuyadevi, R. Shanker, Y. Cui, A. V. Riazanova, M. Järn, M. P. Jonsson and A. J. Svagan, *Adv. Mater.*, 2021, **33**, 2101519.
135. D. Panchal, A. Sharma and S. Pal, *Mater. Today Sustainability*, 2023, **21**, 100264.
136. H. Li, J. Wu, Z. Yin and H. Zhang, *Acc. Chem. Res.*, 2014, **47**, 1067–1075.
137. L. Ottaviano, S. Palleschi, F. Perrozzi, G. D'Olimpio, F. Priante, M. Donarelli, P. Benassi, M. Nardone, M. Gonchigsuren, M. Gombosuren, A. Lucia, G. Moccia and O. A. Cacioppo, *2D Mater.*, 2017, **4**, 045013.

138. X. J. Chua and M. Pumera, *Phys. Chem. Chem. Phys.*, 2017, **19**, 6610–6619.
139. C. L. Choi, J. Feng, Y. Li, J. Wu, A. Zak, R. Tenne and H. Dai, *Nano Res.*, 2013, **6**, 921–928.
140. N. Thomas, S. Mathew, K. M. Nair, K. O'Dowd, P. Forouzandeh, A. Goswami, G. McGranaghan and S. C. Pillai, *Mater. Today Sustainability*, 2021, **13**, 100073.
141. Y. Li, X. Yin and W. Wu, *Ind. Eng. Chem. Res.*, 2018, **57**, 2838–2846.
142. E. D. Grayfer, M. N. Kozlova and V. E. Fedorov, *Adv. Colloid Interface Sci.*, 2017, **245**, 40–61.
143. M. Rajapakse, M. R. K. Musa, D. Vithanage, U. Abu, B. Karki, M. Yu, J. B. Jasinski and G. Sumanasekera, *Ann. Phys.*, 2021, **533**, 1–9.
144. L. Taran and R. Rasuli, *Adv. Powder Technol.*, 2017, **28**, 2996–3003.
145. J. N. Coleman, M. Lotya, A. O'Neill, S. D. Bergin, P. J. King, U. Khan, K. Young, A. Gaucher, S. De, R. J. Smith, I. V. Shvets, S. K. Arora, G. Stanton, H. Y. Kim, K. Lee, G. T. Kim, G. S. Duesberg, T. Hallam, J. J. Boland, J. J. Wang, J. F. Donegan, J. C. Grunlan, G. Moriarty, A. Shmeliov, R. J. Nicholls, J. M. Perkins, E. M. Grieveson, K. Theuwissen, D. W. McComb, P. D. Nellist and V. Nicolosi, *Science*, 2011, **331**, 568–571.
146. Z. Zeng, Z. Yin, X. Huang, H. Li, Q. He, G. Lu, F. Boey and H. Zhang, *Angew. Chem., Int. Ed.*, 2011, **50**, 11093–11097.
147. G. Eda, H. Yamaguchi, D. Voiry, T. Fujita, M. Chen and M. Chhowalla, *Nano Lett.*, 2011, **11**, 5111–5116.
148. M. El Garah, S. Bertolazzi, S. Ippolito, M. Eredia, I. Janica, G. Melinte, O. Ersen, G. Marletta, A. Ciesielski and P. Samorì, *FlatChem*, 2018, **9**, 33–39.
149. S. Park, C. Kim, S. O. Park, N. K. Oh, U. Kim, J. Lee, J. Seo, Y. Yang, H. Y. Lim, S. K. Kwak, G. Kim and H. Park, *Adv. Mater.*, 2020, **32**, 2001889.
150. P. S. Kiran, K. V. Kumar, N. Pandit, S. Indupuri, R. Kumar, V. V. Wagh, A. Islam and A. K. Keshri, *Adv. Funct. Mater.*, 2024, **34**, 2316266.
151. T. Järvinen, G. S. Lorite, J. Peräntie, G. Toth, S. Saarakkala, V. K. Virtanen and K. Kordas, *Nanotechnology*, 2019, **30**, 405501.
152. D. H. Kim, J. C. Park, J. Park, D. Y. Cho, W. H. Kim, B. Shong, J. H. Ahn and T. J. Park, *Chem. Mater.*, 2021, **33**, 4099–4105.
153. H. Yu, M. Liao, W. Zhao, G. Liu, X. J. Zhou, Z. Wei, X. Xu, K. Liu, Z. Hu, K. Deng, S. Zhou, J. A. Shi, L. Gu, C. Shen, T. Zhang, L. Du, L. Xie, J. Zhu, W. Chen, R. Yang, D. Shi and G. Zhang, *ACS Nano*, 2017, **11**, 12001–12007.
154. N. Aspiotis, K. Morgan, B. März, K. Müller-Caspary, M. Ebert, E. Weatherby, M. E. Light, C.-C. Huang, D. W. Hewak, S. Majumdar and I. Zeimpekis, *npj 2D Mater. Appl.*, 2023, **7**, 18.
155. K. P. Loh, *Chem. Mater.*, 2023, **35**, 8771–8773.
156. Z. Wu, T. Shang, Y. Deng, Y. Tao and Q. H. Yang, *Adv. Sci.*, 2020, **7**, 1903077.

157. M. Naguib, V. N. Mochalin, M. W. Barsoum and Y. Gogotsi, *Adv. Mater.*, 2014, **26**, 992–1005.
158. Y. Gogotsi, *Chem. Mater.*, 2023, **35**, 8767–8770.
159. A. V. Mohammadi, J. Rosen and Y. Gogotsi, *Science*, 2021, **372**, eabf1581.
160. Y. Gogotsi and B. Anasori, *ACS Nano*, 2019, **13**, 8491–8494.
161. R. M. Ronchi, J. T. Arantes and S. F. Santos, *Ceram. Int.*, 2019, **45**, 18167–18188.
162. N. Zhang, Y. Hong, S. Yazdanparast and M. Asle Zaeem, *2D Mater.*, 2018, **5**, 045004.
163. M. Khazaei, A. Ranjbar, M. Ghorbani-Asl, M. Arai, T. Sasaki, Y. Liang and S. Yunoki, *Phys. Rev. B: Condens. Matter Mater. Phys.*, 2016, **93**, 205125.
164. M. Khazaei, M. Arai, T. Sasaki, C. Y. Chung, N. S. Venkataramanan, M. Estili, Y. Sakka and Y. Kawazoe, *Adv. Funct. Mater.*, 2013, **23**, 2185–2192.
165. C. Si, K. H. Jin, J. Zhou, Z. Sun and F. Liu, *Nano Lett.*, 2016, **16**, 6584–6591.
166. E. Balcı, Ü. Ö. Akkuş and S. Berber, *Appl. Phys. Lett.*, 2018, **113**(8), 083107.
167. M. Khazaei, A. Ranjbar, M. Arai, T. Sasaki and S. Yunoki, *J. Mater. Chem. C*, 2017, **5**, 2488–2503.
168. X. F. Yu, Y. C. Li, J. B. Cheng, Z. B. Liu, Q. Z. Li, W. Z. Li, X. Yang and B. Xiao, *ACS Appl. Mater. Interfaces*, 2015, **7**, 13707–13713.
169. S. Zhao, W. Kang and J. Xue, *Appl. Phys. Lett.*, 2014, **104**, 133106.
170. A. Champagne and J. C. Charlier, *JPhys Mater.*, 2021, **3**, 032006.
171. J. B. Goodenough, *Scholarpedia*, 2008, **3**, 7382.
172. V. Shukla, *Mater. Adv.*, 2020, **1**, 3104–3121.
173. A. Ono and S. Ishihara, *Phys. Rev. Lett.*, 2017, **119**, 207202.
174. G. Wang, *J. Phys. Chem. C*, 2016, **120**, 18850–18857.
175. Y. Bai, K. Zhou, N. Srikanth, J. H. L. Pang, X. He and R. Wang, *RSC Adv.*, 2016, **6**, 35731–35739.
176. K. Rasool, R. P. Pandey, P. A. Rasheed, S. Buczek, Y. Gogotsi and K. A. Mahmoud, *Mater. Today*, 2019, **30**, 80–102.
177. K. Hantanasirisakul, M.-Q. Zhao, P. Urbankowski, J. Halim, B. Anasori, S. Kota, C. E. Ren, M. W. Barsoum and Y. Gogotsi, *Adv. Electron. Mater.*, 2016, **2**, 1600050.
178. G. R. Berdiyorov, *AIP Adv.*, 2016, **6**, 55105.
179. G. Xu, Y. Niu, X. Yang, Z. Jin, Y. Wang, Y. Xu and H. Niu, *Adv. Opt. Mater.*, 2018, **6**, 1800951.
180. V. Mauchamp, M. Bugnet, E. P. Bellido, G. A. Botton, P. Moreau, D. Magne, M. Naguib, T. Cabioc'h and M. W. Barsoum, *Phys. Rev. B: Condens. Matter Mater. Phys.*, 2014, **89**, 235428.
181. K. Hantanasirisakul and Y. Gogotsi, *Adv. Mater.*, 2018, **30**, 1804779.
182. E. Satheeshkumar, T. Makaryan, A. Melikyan, H. Minassian, Y. Gogotsi and M. Yoshimura, *Sci. Rep.*, 2016, **6**, 32049.

183. D. B. Velusamy, J. K. El-Demellawi, A. M. El-Zohry, A. Giugni, S. Lopatin, M. N. Hedhili, A. E. Mansour, E. Di Fabrizio, O. F. Mohammed and H. N. Alshareef, *Adv. Mater.*, 2019, **31**, 1807658.
184. Y. Peng, P. Cai, L. Yang, Y. Liu, L. Zhu, Q. Zhang, J. Liu, Z. Huang and Y. Yang, *ACS Omega*, 2020, **5**, 26486–26496.
185. B. Fu, J. Sun, C. Wang, C. Shang, L. Xu, J. Li and H. Zhang, *Small*, 2021, **17**, 2006054.
186. J. A. Kumar, P. Prakash, T. Krithiga, D. J. Amarnath, J. Premkumar, N. Rajamohan, Y. Vasseghian, P. Saravanan and M. Rajasimman, *Chemosphere*, 2022, **286**, 131607.
187. V. N. Borysiuk, V. N. Mochalin and Y. Gogotsi, *Nanotechnology*, 2015, **26**, 1–10.
188. V. N. Borysiuk, V. N. Mochalin and Y. Gogotsi, *Comput. Mater. Sci.*, 2018, **143**, 418–424.
189. A. Lipatov, H. Lu, M. Alhabeb, B. Anasori, A. Gruverman, Y. Gogotsi and A. Sinitskii, *Sci. Adv.*, 2018, **4**, 1–7.
190. M. Naguib, T. Saito, S. Lai, M. S. Rager, T. Aytug, M. Parans Paranthaman, M. Q. Zhao and Y. Gogotsi, *RSC Adv.*, 2016, **6**, 72069–72073.
191. M. Naguib, O. Mashtalir, J. Carle, V. Presser, J. Lu, L. Hultman, Y. Gogotsi and M. W. Barsoum, *ACS Nano*, 2012, **6**, 1322–1331.
192. B. Anasori, M. R. Lukatskaya and Y. Gogotsi, *Nat. Rev. Mater.*, 2017, **2**, 16098.
193. O. Mashtalir, K. M. Cook, V. N. Mochalin, M. Crowe, M. W. Barsoum and Y. Gogotsi, *J. Mater. Chem. A*, 2014, **2**, 14334–14338.
194. D. Wu, S. Wang, S. Zhang, J. Yuan, B. Yang and H. Chen, *Phys. Chem. Chem. Phys.*, 2018, **20**, 18924–18930.
195. M. Q. Zhao, C. E. Ren, Z. Ling, M. R. Lukatskaya, C. Zhang, K. L. Van Aken, M. W. Barsoum and Y. Gogotsi, *Adv. Mater.*, 2015, **27**, 339–345.
196. P. Chakraborty, T. Das, D. Nafday, L. Boeri and T. Saha-Dasgupta, *Phys. Rev. B: Condens. Matter Mater. Phys.*, 2017, **95**, 184106.
197. H. Mahmud, J. U. Ahamed and M. N. I. Khan, *Mater. Res. Express*, 2022, **9**, 112001.
198. V. M. Hong Ng, H. Huang, K. Zhou, P. S. Lee, W. Que, J. Z. Xu and L. B. Kong, *J. Mater. Chem. A*, 2017, **5**, 3039–3068.
199. W. Sun, S. A. Shah, Y. Chen, Z. Tan, H. Gao, T. Habib, M. Radovic and M. J. Green, *J. Mater. Chem. A*, 2017, **5**, 21663–21668.
200. A. Champagne and J.-C. Charlier, *JPhys Mater.*, 2020, **3**, 032006.
201. A. Gkountaras, Y. Kim, J. Coraux, V. Bouchiat, S. Lisi, M. W. Barsoum and T. Ouisse, *Small*, 2020, **16**, 1905784.
202. R. Verma, A. Sharma, V. Dutta, A. Chauhan, D. Pathak and S. Ghotekar, *Emergent Mater.*, 2024, **7**, 35–62.
203. R. Ma and T. Sasaki, *Acc. Chem. Res.*, 2015, **48**, 136–143.
204. N. Uetake, F. Kawamura and H. Yusa, *J. Nucl. Sci. Technol.*, 1989, **26**, 270–277.
205. O. Salim, K. A. Mahmoud, K. K. Pant and R. K. Joshi, *Mater. Today Chem.*, 2019, 14.

206. O. Mashtalir, M. Naguib, V. N. Mochalin, Y. Dall'Agnese, M. Heon, M. W. Barsoum and Y. Gogotsi, *Nat. Commun.*, 2013, **4**, 1716.
207. K. A. Papadopoulou, A. Chroneos, D. Parfitt and S.-R. G. Christopoulos, *J. Appl. Phys.*, 2020, **128**, 170902.
208. C. Xu, L. Wang, Z. Liu, L. Chen, J. Guo, N. Kang, X. L. Ma, H. M. Cheng and W. Ren, *Nat. Mater.*, 2015, **14**, 1135–1141.
209. X. Zhao, W. Sun, D. Geng, W. Fu, J. Dan, Y. Xie, P. R. C. Kent, W. Zhou, S. J. Pennycook and K. P. Loh, *Adv. Mater.*, 2019, **31**, 1808343.
210. D. C. Geng, X. X. Zhao, Z. X. Chen, W. W. Sun, W. Fu, J. Y. Chen, W. Liu, W. Zhou and K. P. Loh, *Adv. Mater.*, 2017, **29**, 1700072.
211. F. Zhang, Z. Zhang, H. Wang, C. H. Chan, N. Y. Chan, X. X. Chen and J.-Y. Dai, *Phys. Rev. Mater.*, 2017, **1**, 034002.
212. B. Anasori and Y. Gogotsi, *2D Metal Carbides and Nitrides (MXenes)*, 2019, pp. 3–12.
213. A. K. Fard, G. Mckay, R. Chamoun, T. Rhadfi, H. Preud'Homme and M. A. Atieh, *Chem. Eng. J.*, 2017, **317**, 331–342.
214. Y. Ying, Y. Liu, X. Wang, Y. Mao, W. Cao, P. Hu and X. Peng, *ACS Appl. Mater. Interfaces*, 2015, **7**, 1795–1803.
215. X. Xie, C. Chen, N. Zhang, Z. R. Tang, J. Jiang and Y. J. Xu, *Nat. Sustainability*, 2019, **2**, 856–862.
216. B. M. Jun, M. Jang, C. M. Park, J. Han and Y. Yoon, *Nucl. Eng. Technol.*, 2020, **52**, 1201–1207.
217. A. R. Khan, S. M. Husnain, F. Shahzad, S. Mujtaba-Ul-Hassan, M. Mehmood, J. Ahmad, M. T. Mehran and S. Rahman, *Dalton Trans.*, 2019, **48**, 11803–11812.
218. L. Wang, H. Song, L. Yuan, Z. Li, Y. Zhang, J. K. Gibson, L. Zheng, Z. Chai and W. Shi, *Environ. Sci. Technol.*, 2018, **52**, 10748–10756.
219. F. Meng, M. Seredych, C. Chen, V. Gura, S. Mikhalovsky, S. Sandeman, G. Ingavle, T. Ozulumba, L. Miao, B. Anasori and Y. Gogotsi, *ACS Nano*, 2018, **12**, 10518–10528.
220. L. Wu, X. Lu, Dhanjai, Z. S. Wu, Y. Dong, X. Wang, S. Zheng and J. Chen, *Biosens. Bioelectron.*, 2018, **107**, 69–75.
221. S. Kim, F. Gholamirad, M. Yu, C. M. Park, A. Jang, M. Jang, N. Taheri-Qazvini and Y. Yoon, *Chem. Eng. J.*, 2021, **406**, 126789.
222. Z. Wei, Z. Peigen, T. Wubian, Q. Xia, Z. Yamei and S. ZhengMing, *Mater. Chem. Phys.*, 2018, **206**, 270–276.
223. Y. Zhang, Z. Zhou, J. Lan and P. Zhang, *Appl. Surf. Sci.*, 2019, **469**, 770–774.
224. P. R. Anusuyadevi, S. Pranavi, D. J. P. Kumar, Y. Misra, S. S. Mentha, P. Gonugunta, P. Taheri and A. Mol, in *Towards Sustainable and Green Hydrogen Production by Photocatalysis: Scalability Opportunities and Challenges*, 2024, vol. 1, pp. 137–164.
225. Y. Li, X. Deng, J. Tian, Z. Liang and H. Cui, *Appl. Mater. Today*, 2018, **13**, 217–227.
226. T. Su, R. Peng, Z. D. Hood, M. Naguib, I. N. Ivanov, J. K. Keum, Z. Qin, Z. Guo and Z. Wu, *ChemSusChem*, 2018, **11**, 688–699.

227. C. Peng, P. Wei, X. Li, Y. Liu, Y. Cao, H. Wang, H. Yu, F. Peng, L. Zhang, B. Zhang and K. Lv, *Nano Energy*, 2018, **53**, 97–107.
228. Y. Li, Z. Yin, G. Ji, Z. Liang, Y. Xue, Y. Guo, J. Tian, X. Wang and H. Cui, *Appl. Catal., B*, 2019, **246**, 12–20.
229. R. Xiao, C. Zhao, Z. Zou, Z. Chen, L. Tian, H. Xu, H. Tang, Q. Liu, Z. Lin and X. Yang, *Appl. Catal., B*, 2020, **268**, 118382.
230. L. F. Hong, R. T. Guo, Y. Yuan, X. Y. Ji, Z. S. Li, Z. D. Lin and W. G. Pan, *Mater. Today Energy*, 2020, **18**, 100521.
231. H. Wang, Y. Sun, Y. Wu, W. Tu, S. Wu, X. Yuan, G. Zeng, Z. J. Xu, S. Li and J. W. Chew, *Appl. Catal., B*, 2019, **245**, 290–301.
232. L. Cheng, Q. Chen, J. Li and H. Liu, *Appl. Catal., B*, 2020, **267**, 118379.
233. D. Ruan, M. Fujitsuka and T. Majima, *Appl. Catal., B*, 2020, **264**, 118541.
234. L. Biswal, S. Nayak and K. Parida, *Catal. Sci. Technol.*, 2021, **11**, 1222–1248.
235. P. Lin, J. Shen, X. Yu, Q. Liu, D. Li and H. Tang, *Ceram. Int.*, 2019, **45**, 24656–24663.
236. M. Tahir, A. Ali Khan, S. Tasleem, R. Mansoor and W. K. Fan, *Energy Fuels*, 2021, **35**, 10374–10404.
237. J. Li, Z. Wang, H. Chen, Q. Zhang, H. Hu, L. Liu, J. Ye and D. Wang, *Catal. Sci. Technol.*, 2021, **11**, 4953–4961.
238. X. Li, Y. Bai, X. Shi, J. Huang, K. Zhang, R. Wang and L. Ye, *Appl. Surf. Sci.*, 2021, **546**, 149111.
239. X. Xie, M. Q. Zhao, B. Anasori, K. Maleski, C. E. Ren, J. Li, B. W. Byles, E. Pomerantseva, G. Wang and Y. Gogotsi, *Nano Energy*, 2016, **26**, 513–523.
240. V. Natu, M. Clites, E. Pomerantseva and M. W. Barsoum, *Mater. Res. Lett.*, 2018, **6**, 230–235.
241. C. E. Ren, M. Q. Zhao, T. Makaryan, J. Halim, M. Boota, S. Kota, B. Anasori, M. W. Barsoum and Y. Gogotsi, *ChemElectroChem*, 2016, **3**, 689–693.
242. M. R. Lukatskaya, S. Kota, Z. Lin, M.-Q. Zhao, N. Shpigel, M. D. Levi, J. Halim, P.-L. Taberna, M. W. Barsoum, P. Simon and Y. Gogotsi, *Nat. Energy*, 2017, **2**, 17105.
243. Technology Roadmap – Hydrogen and Fuel Cells, IEA, Paris, 2015.
244. X. Xie, L. Du, L. Yan, S. Park, Y. Qiu, J. Sokolowski, W. Wang and Y. Shao, *Adv. Funct. Mater.*, 2022, **32**, 2110036.
245. Y. Kim, E. Choi, S. Kim and H. R. Byon, *Chem. Sci.*, 2023, **14**, 10644–10663.
246. M. Chatenet, B. G. Pollet, D. R. Dekel, F. Dionigi, J. Deseure, P. Millet, R. D. Braatz, M. Z. Bazant, M. Eikerling, I. Staffell, P. Balcombe, Y. Shao-Horn and H. Schäfer, *Chem. Soc. Rev.*, 2022, **51**, 4583–4762.
247. N. Mahmood, I. A. De Castro, K. Pramoda, K. Khoshmanesh, S. K. Bhargava and K. Kalantar-Zadeh, *Energy Storage Mater.*, 2019, **16**, 455–480.
248. Z. Lei, J. M. Lee, G. Singh, C. I. Sathish, X. Chu, A. H. Al-Muhtaseb, A. Vinu and J. Yi, *Energy Storage Mater.*, 2021, **36**, 514–550.

249. H. van Gog, W.-F. Li, C. Fang, R. S. Koster, M. Dijkstra and M. van Huis, *npj 2D Mater. Appl.*, 2019, **3**, 18.
250. N. Bahlawane and D. Lenoble, *Chem. Vap. Deposition*, 2014, **20**, 299–311.
251. Y. Meng, W. Song, H. Huang, Z. Ren, S.-Y. Chen and S. L. Suib, *J. Am. Chem. Soc.*, 2014, **136**, 11452–11464.
252. H. Ding, K. G. Ray, V. Ozolins and M. Asta, *Phys. Rev. B: Condens. Matter Mater. Phys.*, 2012, **85**, 12104.
253. B. Y. Zhang, K. Xu, Q. Yao, A. Jannat, G. Ren, M. R. Field, X. Wen, C. Zhou, A. Zavabeti and J. Z. Ou, *Nat. Mater.*, 2021, **20**, 1073–1078.
254. M. Singh, E. D. Gaspera, T. Ahmed, S. Walia, R. Ramanathan, J. van Embden, E. Mayes and V. Bansal, *2D Mater.*, 2017, **4**, 025110.
255. W. Hua, Z. Wu, M. Chen, M. Knapp, X. Guo, S. Indris, J. R. Binder, N. N. Bramnik, B. Zhong, H. Guo, S. Chou, Y.-M. Kang and H. Ehrenberg, *J. Mater. Chem. A*, 2017, **5**, 25391–25400.
256. D. Hanlon, C. Backes, T. M. Higgins, M. Hughes, A. O'Neill, P. King, N. McEvoy, G. S. Duesberg, B. Mendoza Sanchez, H. Pettersson, V. Nicolosi and J. N. Coleman, *Chem. Mater.*, 2014, **26**, 1751–1763.
257. C. Tan, X. Cao, X.-J. Wu, Q. He, J. Yang, X. Zhang, J. Chen, W. Zhao, S. Han, G.-H. Nam, M. Sindoro and H. Zhang, *Chem. Rev.*, 2017, **117**, 6225–6331.
258. X. Rui, Z. Lu, H. Yu, D. Yang, H. H. Hng, T. M. Lim and Q. Yan, *Nanoscale*, 2013, **5**, 556–560.
259. Z. Tan, K. Sato and S. Ohara, *Adv. Powder Technol.*, 2015, **26**, 296–302.
260. T. Zhang, Z. Zhu, H. Chen, Y. Bai, S. Xiao, X. Zheng, Q. Xue and S. Yang, *Nanoscale*, 2015, **7**, 2933–2940.
261. B. Y. Zhang, A. Zavabeti, A. F. Chrimes, F. Haque, L. A. O'Dell, H. Khan, N. Syed, R. Datta, Y. Wang, A. S. R. Chesman, T. Daeneke, K. Kalantar-zadeh and J. Z. Ou, *Adv. Funct. Mater.*, 2018, **28**, 1706006.
262. X. Ju, P. Ning, X. Tong, X. Lin, X. Pan, Q. Li, X. Duan and T. Wang, *Electrochim. Acta*, 2016, **213**, 641–647.
263. J. Zou, H. Zeng, Y. Wang and Y. Li, *Phys. Status Solidi RRL*, 2018, **12**, 1700439.
264. Z. Shi, J. Liu, Y. Gao and Y. Xu, *J. Mater. Sci.*, 2021, **56**, 1612–1629.
265. M. You, W. Zhang, X. Yan, H. Jiang, J. Miao, Y. Li, W. Zhou, Y. Zhu and X. Cheng, *Ceram. Int.*, 2021, **47**, 3337–3345.
266. Z. Song, Y. Zhang, W. Liu, S. Zhang, G. Liu, H. Chen and J. Qiu, *Electrochim. Acta*, 2013, **112**, 120–126.
267. Z. Sun, T. Liao, Y. Dou, S. M. Hwang, M.-S. Park, L. Jiang, J. H. Kim and S. X. Dou, *Nat. Commun.*, 2014, **5**, 3813.
268. Y. Lin and J. W. Connell, *Nanoscale*, 2012, **4**, 6908.
269. G. Bottari, M. Á. Herranz, L. Wibmer, M. Volland, L. Rodríguez-Pérez, D. M. Guldi, A. Hirsch, N. Martín, F. D'Souza and T. Torres, *Chem. Soc. Rev.*, 2017, **46**, 4464–4500.
270. K. Ba, W. Jiang, J. Cheng, J. Bao, N. Xuan, Y. Sun, B. Liu, A. Xie, S. Wu and Z. Sun, *Sci. Rep.*, 2017, **7**, 45584.

271. Q. Peng, W. Ji and S. De, *Comput. Mater. Sci.*, 2012, **56**, 11–17.
272. A. Falin, Q. Cai, E. J. G. Santos, D. Scullion, D. Qian, R. Zhang, Z. Yang, S. Huang, K. Watanabe, T. Taniguchi, M. R. Barnett, Y. Chen, R. S. Ruoff and L. H. Li, *Nat. Commun.*, 2017, **8**, 15815.
273. A. Pakdel, Y. Bando and D. Golberg, *Chem. Soc. Rev.*, 2014, **43**, 934–959.
274. R. T. Paine and C. K. Narula, *Chem. Rev.*, 1990, **90**, 73–91.
275. K. Zhang, Y. Feng, F. Wang, Z. Yang and J. Wang, *J. Mater. Chem. C*, 2017, **5**, 11992–12022.
276. C. R. Dean, A. F. Young, I. Meric, C. Lee, L. Wang, S. Sorgenfrei, K. Watanabe, T. Taniguchi, P. Kim, K. L. Shepard and J. Hone, *Nat. Nanotechnol.*, 2010, **5**, 722–726.
277. K. K. Kim, A. Hsu, X. Jia, S. M. Kim, Y. Shi, M. Dresselhaus, T. Palacios and J. Kong, *ACS Nano*, 2012, **6**, 8583–8590.
278. K. H. Lee, H.-J. Shin, J. Lee, I. Lee, G.-H. Kim, J.-Y. Choi and S.-W. Kim, *Nano Lett.*, 2012, **12**, 714–718.
279. J. Li, S. Majety, R. Dahal, W. P. Zhao, J. Y. Lin and H. X. Jiang, *Appl. Phys. Lett.*, 2012, **101**, 171112.
280. L. H. Li, E. J. G. Santos, T. Xing, E. Cappelluti, R. Roldán, Y. Chen, K. Watanabe and T. Taniguchi, *Nano Lett.*, 2015, **15**, 218–223.
281. G. Shi, Y. Hanlumyuang, Z. Liu, Y. Gong, W. Gao, B. Li, J. Kono, J. Lou, R. Vajtai, P. Sharma and P. M. Ajayan, *Nano Lett.*, 2014, **14**, 1739–1744.
282. A. Laturia, M. L. Van de Put and W. G. Vandenberghe, *npj 2D Mater. Appl.*, 2018, **2**, 6.
283. P. S. Das and A. Biswas, *Microelectron. Reliab.*, 2010, **50**, 1924–1930.
284. L. Britnell, R. V. Gorbachev, R. Jalil, B. D. Belle, F. Schedin, M. I. Katsnelson, L. Eaves, S. V. Morozov, A. S. Mayorov, N. M. R. Peres, A. H. Castro Neto, J. Leist, A. K. Geim, L. A. Ponomarenko and K. S. Novoselov, *Nano Lett.*, 2012, **12**, 1707–1710.
285. G. Chilkoor, S. P. Karanam, S. Star, N. Shrestha, R. K. Sani, V. K. K. Upadhyayula, D. Ghoshal, N. A. Koratkar, M. Meyyappan and V. Gadhamshetty, *ACS Nano*, 2018, **12**, 2242–2252.
286. N. Goel and M. Kumar, *J. Mater. Chem. C*, 2021, **9**, 1537–1549.
287. N. Hakimi Raad, N. Manavizadeh, I. Frank and E. Nadimi, *Appl. Surf. Sci.*, 2021, **565**, 150454.
288. A. F. Khan, D. A. C. Brownson, E. P. Randviir, G. C. Smith and C. E. Banks, *Anal. Chem.*, 2016, **88**, 9729–9737.
289. Y. Lu, B. Li, N. Xu, Z. Zhou, Y. Xiao, Y. Jiang, T. Li, S. Hu, Y. Gong and Y. Cao, *Nat. Commun.*, 2023, **14**, 6965.
290. P. Marbaniang, I. Patil, M. Lokanathan, H. Parse, D. Catherin Sesu, S. Ingavale and B. Kakade, *ACS Sustainable Chem. Eng.*, 2018, **6**, 11115–11122.
291. M. J. Molaei, M. Younas and M. Rezakazemi, *ACS Appl. Electron. Mater.*, 2021, **3**, 5165–5187.
292. R. Szostak, A. Morais, S. A. Carminati, S. V. Costa, P. E. Marchezi and A. F. Nogueira, in *The Future of Semiconductor Oxides in Next-Generation Solar Cells*, Elsevier, 2018, pp. 395–437.

293. A. Kuc and T. Heine, *Chem. Soc. Rev.*, 2015, **44**, 2603–2614.
294. A. Kuc, N. Zibouche and T. Heine, *Phys. Rev. B: Condens. Matter Mater. Phys.*, 2011, **83**, 245213.
295. W. Sun, S. A. Shah, Y. Chen, Z. Tan, H. Gao, T. Habib, M. Radovic and M. J. Green, *J. Mater. Chem. A*, 2017, **5**, 21663–21668.
296. Y. Gogotsi, *Nat. Mater.*, 2015, **14**, 1079–1080.
297. N. Izyumskaya, D. O. Demchenko, S. Das, Ü. Özgür, V. Avrutin and H. Morkoç, *Adv. Electron. Mater.*, 2017, **3**, 1600485.